

2015

Gully volume estimates using  
UAV Photometry in the  
Salagou area

S.C. Verdonk (4005236)

University of Utrecht

4/13/2015

## Table of contents

Abstract .....	3
List of abbreviations .....	3
Chapter 1: Introduction.....	4
1.1 Context .....	4
1.2 Research questions.....	5
1.3 Report layout.....	5
Chapter 2: Literature review .....	6
2.1 Study area.....	6
2.2 Gully erosion.....	12
2.3 Unmanned Aerial Vehicles .....	19
2.4 Photometry.....	25
Chapter 3: Methods .....	34
3.1 Gathering data.....	34
3.2 DEM building .....	39
3.3 Obtaining gully volumes .....	43
chapter 4: Results and Discussion .....	49
4.1 Gully discriptions and results .....	49
4.3 Discussion on optimal settings .....	62
4.4 Discussion on volume estimates .....	63
5 Conclusions & recommendations.....	64
Appendix A: Applications of UAVs.....	65
Appendix B: Python script for DEM statistics.....	66
Appendix C: Gully result tables .....	68
Appendix D: Vailhes gully orthophoto .....	70
Appendix E: Salagou gully orthophoto .....	71
Appendix F: Celles gully orthophoto .....	72
Appendix G: Brenas gully orthophoto .....	73
Appendix H: Test run statistics (entire DEM) .....	74
Appendix i: Test run statistics (gully bottom).....	75
Appendix J: Preparing CSV files .....	75
References.....	76

## Abstract

The Area around lake Salagou in the south of France has been experiencing significant fluvial erosion in the form of gullying since the last glacial maximum. With the aim of creating a better understanding of long-term erosion rates the volumes of some of these gullies have been calculated. Using aerial images acquired from a UAV platform and DGPS measurements DEMs of four gullies were made in Agisoft Photoscan. From these DEMs the vegetation was removed and the gully volumes were calculated using several GIS algorithms. Accuracy analysis revealed a lot of variability of accuracy with respect to internal gully relief. Overall the accuracy were on par with those of other studies which utilized UAV photometry. The gully volumes range from  $10.95 \times 10^4$  cubic meters for the largest gully and  $1.17 \times 10^4$  cubic meters for the smallest gully, that were measured.

## List of abbreviations

CSV	Comma/character separated values
DEM	Digital elevation model
DTM	Digital terrain model (vegetation removed)
DSM	Digital surface model
DGPS	Differential global positioning system
GCP	Ground control point
GCS	Ground control station
GIS	Geographical information system
MVS	Multi-view stereo
RTK	Real-time kinetic
SfM	Structure from motion
LiDAR	Light detection and ranging
INS	Internal navigation system
VTOL	Vertical takeoff and landing
UAV	Unmanned aerial vehicle

# Chapter 1: Introduction

## 1.1 Context

### *Gully erosion*

Gullies are a form runoff-water induced linear erosion which can have various causes, related to geology and precipitation. Gullies are characterized by steep side walls perpendicular to the slope direction; and they tend to carry water during and after large precipitation events. Poesen et al. (2002) stresses the need for additional research into gully erosion, which contributes between 50 to 80 percent of the total erosion in arid and semi-arid environments. The increased drainage which gullies provide will often increase aridification in the surrounding area. Contemporary land use change has greatly increased the occurrence of ephemeral gullies which are often hazardous to agriculture. Gully dynamics can be seen as a proxy for climate change because gully development depends on precipitation volume and intensity (Poesen, 2003).

Quantifying gully erosion has always been a difficult process due to the complex dynamic geomorphologic development of gully systems. Topography is a major factor affecting gully dynamics. Detailed representations by accurate digital elevation models can provide a better understanding of gully dynamics. Marzloff & Poesen (2009) have created detailed digital elevation models (DEMs) of ephemeral U-shaped gullies using an airborne sensor platform in 2000 and 2007. By comparing the two DEMs temporal volumetric changes and erosion rates can be calculated.

### *UAV Photometry*

Recent developments in the fields of unmanned aerial vehicles (UAVs) and computer vision have paved the way for low cost on demand high accuracy DEM acquisition. Photometry is the process of creating a 3D representation of a scene using overlapping images taken from the same camera, in this case mounted on a UAV. Eissenbeiss (2009) made a doctoral dissertation on UAV photometry which stressed the need of ground control points to improve the accuracy of georeferencing and DEM generation. In addition accurate exterior orientation values given by the inertial navigation system of the UAV are an important factor of the accuracy of the resulting DEM. However, it is hard to fit and work with accurate DGPS on the UAV itself, therefore the exterior orientation is often the limiting factor of the DEM accuracy. Ground control points are used as a reference for the Helmert transformation which applies a real world coordinate system to the DEM and to improve the accuracy of the point cloud computation. These are points in the imagery which have been highlighted in the field and measured using RTK GPS. Digital elevation models acquired using UAV photometry are on par with LiDAR systems when it comes to both horizontal and vertical accuracy (Hughenholtz, 2013). In addition the UAV photometry method is considerably cheaper. Accuracy achieved with UAV photometry using conventional digital cameras are in the sub-decimeter range.

## *Geomorphology of Salagou*

The area around Salagou in the south of France is a type of badland landscape which is well suited for research into gullies using UAV photometry. Its geology and climate led to the formation of large longterm gullies, which impede agricultural developments causing distress to the population. Bonnet et al. (2001) did a comprehensive study into the geomorphologic development of the Salagou area. It was concluded that three geomorphologic stages could be identified. The gullies are the latest stage, which resulted from fluvial erosion during the current interglacial. They are cut into the remnants of periglacial colluviums which are of glacial age. The first state consists of basaltic outflows which are now at the top of the relief due to a relief inversion. Measuring the gully volumes should yield the erosion rates since the last glacial maximum.

## **1.2 Research questions**

The aims of this research are to explore the possibilities for accurate calculations of gully volumes using UAV photometry. It has been subdivided into several research questions.

### **How much sediment has been eroded since the development of the gullies after the last glacial maximum?**

- What kind of GIS processing methods can be used for gully volume calculations?
- How does the UAV photometry method for monitoring gully erosion compare to other gully methods?

### **How can the most accurate digital terrain models be made using UAV photometry of large V-shaped gullies?**

- How accurate is the UAV photometry compared to reference points acquired using RTK DGPS?
- How do the errors in the DEM relate to different parts of a gully system?
- How do the results of this study stand up to the accuracies measured in previous studies?

## **1.3 Report layout**

In chapter 2 an extensive review of the literature of the subject will be given. It will focus on the details of the gullies and the field work area. And on the methodology of using UAVs in remote sensing and the intricacies of using them for photogrammetry. Chapter 3, the method section consists of three parts: the method of data acquisition in the field, the DEM and orthophoto creation process, GIS processing methods to remove the vegetation and calculate the volume. Chapter 4 , The results and the discussion includes the gully descriptions, and their DEMs, accuracies and volumes which are described and elaborated upon. In addition the accuracies are compared to those of other studies, and the methods are discussed. And finally, chapter 5 gives the conclusions and recommendations for further research.

## Chapter 2: Literature review

### 2.1 Study area

#### *Basin de Lodève*

The study area is situated in southern France in the region Languedoc-Roussillon, department Hérault. It is located inside the Salagou basin south of the town of Lodève and west of Bédarieux, see Figure 1. Inside the basin there are several smaller hamlets, the largest of which are Octon and Salasc. The area consist of a horse shoe shaped valley draining eastwards into Salagou river which drains into the Salagou lake. The route national flanks the fieldwork area in the south while the E11 highway passes through Lodève and continues east of the Salagou lake, a minor road runs along the valley floor. The lake has an altitude of about 140 meters amsl; the highest points are on the flanks of the valley on the north side, they are in excess of 500 meters amsl, the highest points of the southern range are in excess of 450 meters. There is a general trend of elevation increase from east to west. In the northwestern corner a saddle, with an elevation of 380 meters, divides the Salagou catchment from a neighboring catchment.

In the region agricultural activities are significantly hampered by gully, rill and sheet erosion. The lake turns red after heavy showers this indicates high erosion rates of the red sedimentary rocks (leenheer, 2006). On the sides of the valley steep gullies have incised into the flanks further indicating the state of total erosion which this area experiences. Most of them are orientated north to south.

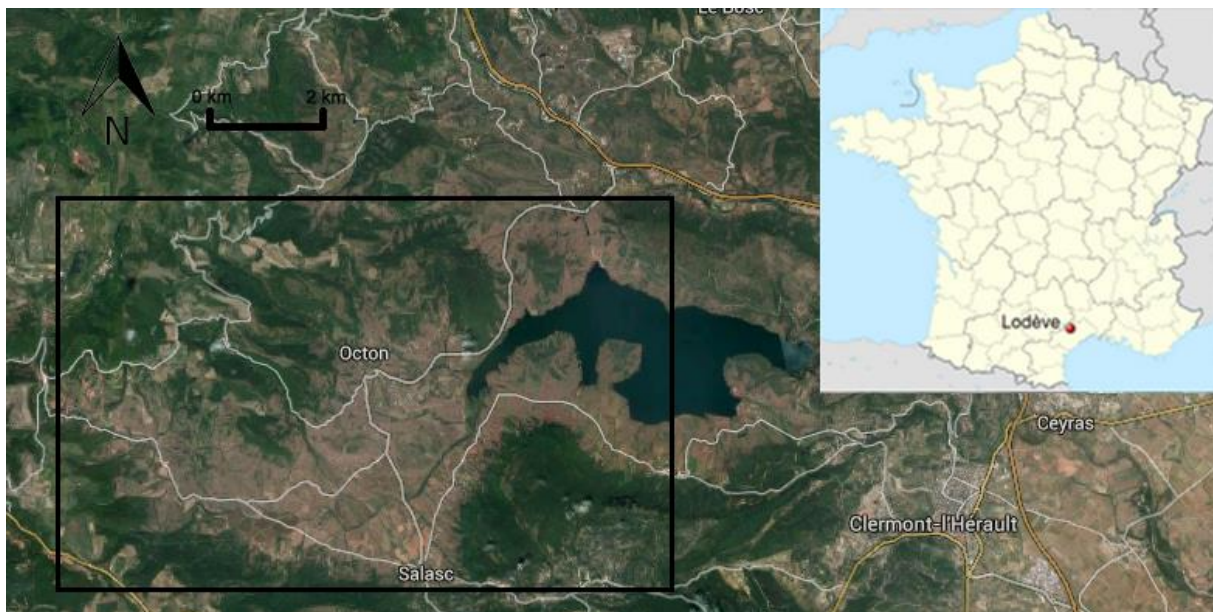


Figure 1, location of the fieldwork area in France

## Geology

The geologic region of the Lodève Basin is a continental half-graben structure of Permian age (Gastaud et al, 1983). The basement consists of Permian siltstones, minor sandstones and red pelites, see Figure 3, which were deposited in a fluvio-lacustrine environment. This formation has been the subject of several studies in paleontology (Evans, 2012) and paleoclimatology (Sneider et al., 2006),. The characteristic red colouring of the basement is the result of its high iron oxide content. The Permian sedimentary rocks have been tilted 15° to 30° degrees southwards as a result reactivation of listric faults during the collapse Hercynian orogeny. Some of the strata have been deposited syntectonically (during the tectonic activity). Afterwards Mesozoic strata have been deposited horizontally consisting predominantly of sandstones. These Mesozoic rocks have been mostly eroded in the research area laying bare the Permian sediments (Van der Zee et al., 2008). Figure 4 shows a basic geologic map of the area.

After a large hiatus, the next part of the rock record in the area are the Quarternary basaltic outflows, which were deposited as a result of volcanic activity in the early Pleistocene (Gastaud et al., 1983). The basalts would have originally been found in the valleys, however due to erosion of the softer surrounding sedimentary rocks they can now be found in the highest parts of the landscape. The basalt ridges trigger the development of the gullies; as the basalts are hard, impervious to erosion, whereas the underlying siltstones are soft. Figure 2 shows a north to south orientated geologic profile to the east of the field work area, basaltic outflows are clearly visible above the south sloping Permian sediments.

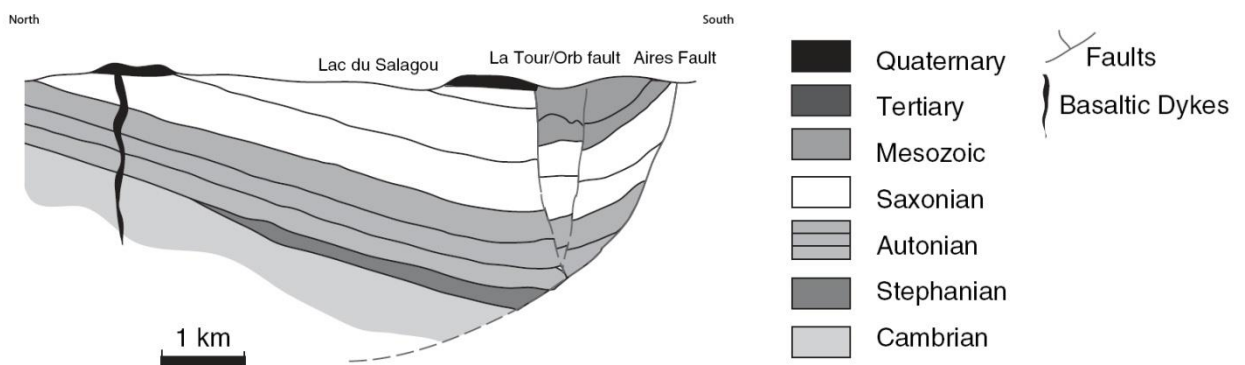


Figure 2, a geologic profile centered around the Salagou lake (modified after van der Zee et al. 2008)



Figure 3, the red pelites exhibit a state of total erosion

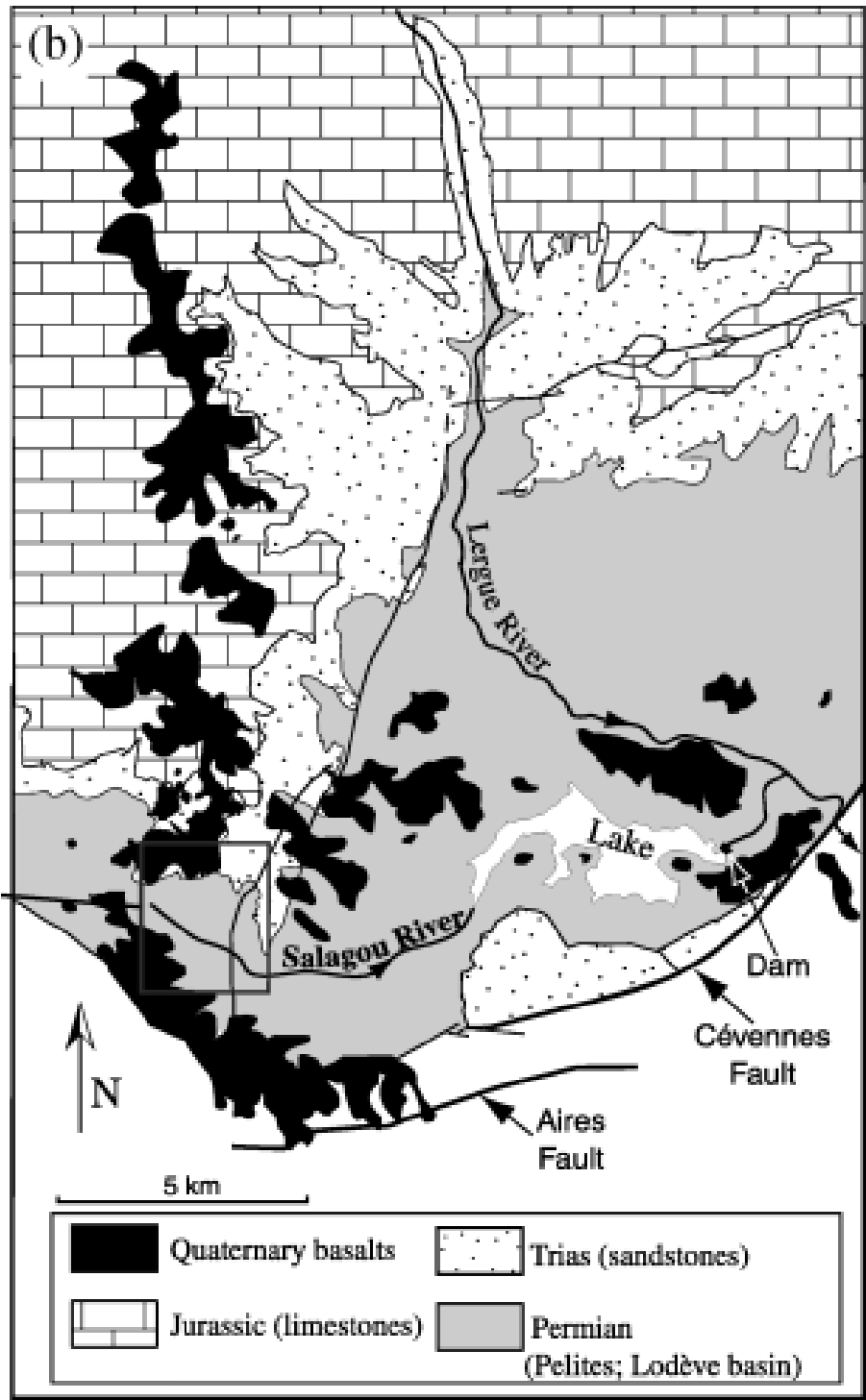


Figure 4, A geologic map of the Lodève area, obtained from Bonnet et al. (2001). The square indicates the field work area for the study of Bonnet, The gullies studied in this project are found on the north side of the Salagou river and lake



## Geomorphology

An extensive study into the geomorphology of the Lodeve Basin has been conducted by Bonnet et al. (2001). They identified three different geomorphologic stages, an overview of them is presented in Table 1, An overview of the geomorphological stages, after Bonnet et al. (2001). and Figure 5.

The first geomorphologic stage is found on top of the hard basaltic outcrops which occur at the highest level in the landscape. The basalt originally flowed down to the bottom of the paleolandscape. However, due to subsequent erosion of its surroundings it can be found at the top of the current day landscape at an elevation of up to 400 meters. Since these basalts are found on top of each other, with the younger outflows above the older ones and not side by side as would have been expected if erosion took place, it is assumed that there have been no significant episodes of vertical erosion between the volcanic phases. So the vertical erosion which caused the relief inversion must have occurred after the final volcanic phase (bonnet et al., 2001). underneath the hard basaltic outcrops older geomorphology is preserved which is only visible at the edges of the basalts. It consists of a relatively flat area with a relief of up to 5 meters which is the result of the occurrence of small paleogullies.

The bottom of the second stage is found 100 to 150 meters below the first stage at an height of about 300 meters amsl. Its geomorphology consists of concave up convergent erosional features with colluvium deposits at its base. This is indicative of an unchanneled valley where mass wasting of the hill slopes was the dominant erosive process. Figure 6 shows an DEM interpreted in GIS, which represents the second stage. During the last glacial period there would have been an ice sheet covering the central massif to the north (Buoncristiani & Campi, 2004) and this region would have been subjected to arid periglacial conditions with a dry and windy climate.

The third geomorphologic stage cuts through the second stage in many locations. At the top of reincision, at the boundary of the second and third stage, characteristic nick points can be found. The third stage can be found at an height of about 250 meters amsl, with the top 150 meters below the first stage and its base 50 meters lower on the valley floor. Its geomorphology consists of fluvial gullies (see chapter 2.2 for more information on gullies) draining in to the Salagou lake. See Figure 7 for a satellite image of the gullies. The gullies are currently in a total erosive state. Its fluvial morphology suggest that it has been formed during the current Holocene interglacial which has much wetter conditions then the preceding Weichselien glacial.

It can be assumed that the long term erosion to which the area has been subjected has been the result of an alternation between colluvium mass wasting processes during glacials and alluvium gully formation during interglacials. However there is no evidence to support this because older stages have not been preserved.

**Table 1, An overview of the geomorphological stages, after Bonnet et al. (2001).**

	Relative Height	Geomorphology	Estimated age
Stage 1	Highest	Relatively flat with small gullies up to meters	1.06 Ma (gastaud et al., 1983)
Stage 2	Middle	Remnants of mass wasting processes, gentle sloping valleys with colluvium	Start of the Holocene, $\pm$ 12 Ka
Stage 3	Lowest	Heavily incised V-shaped gullies up to 50 meters deep	Contemporary

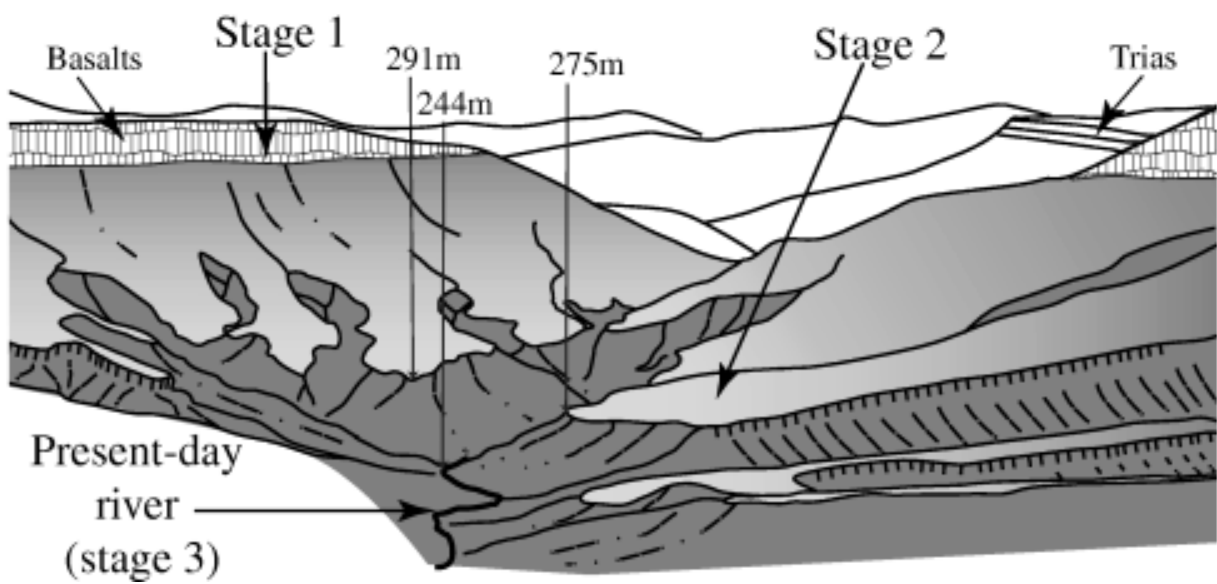


Figure 5, a panoramic picture of the gullies west of lake Salagou and a schematic representation of the picture showing the different geomorphologic stages. ( Bonnet et al., 2001).

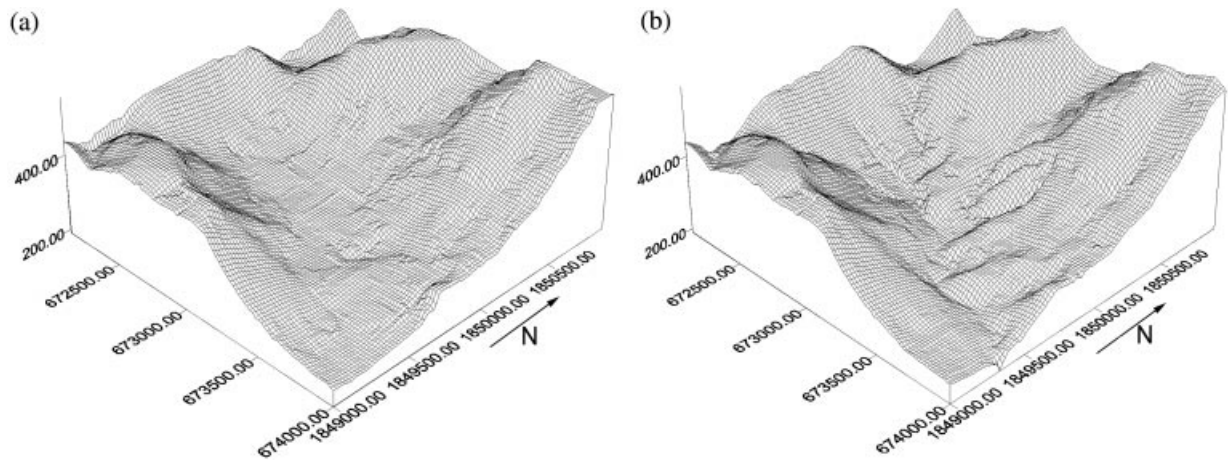


Figure 6, DEMs of estimated second stage (left) and measured third stage (right), (Bonnet et al., 2001).

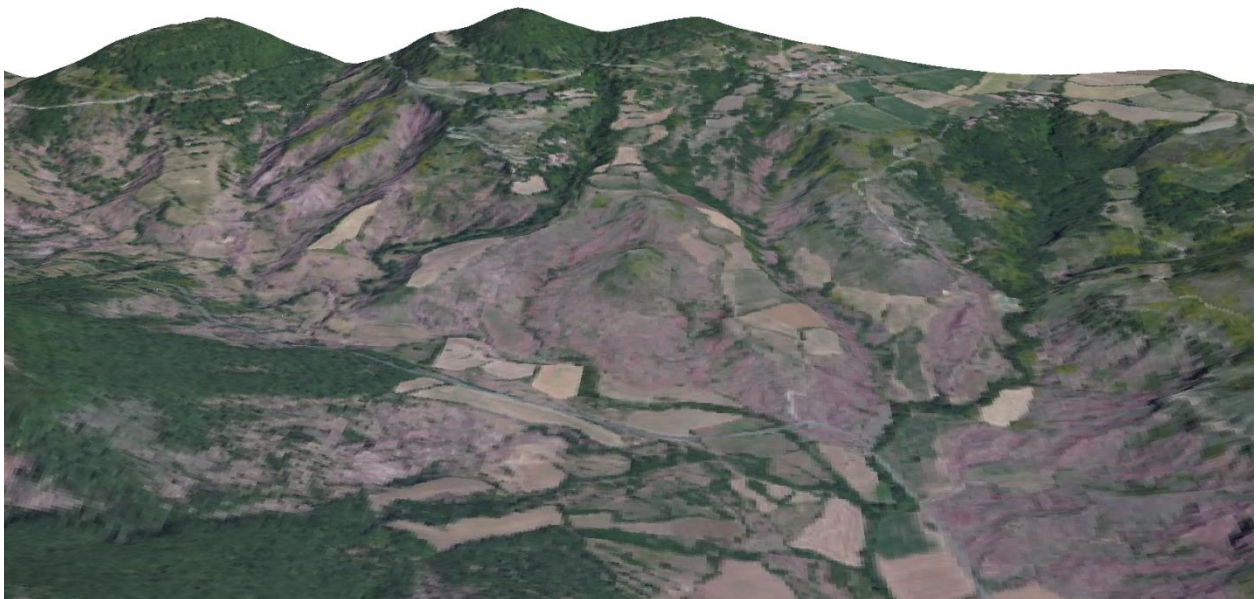


Figure 7, a 3D representation of the gullies and hills in the northern Salagou valley. Note the incision in the second stage. The first stage is poorly visible. Acquired from Google earth images overlaid on a low resolution DEM in ARCScene.

### *Climate*

The study area currently experiences Mediterranean climatic conditions characterized by warm summers and mild winters. During summer the near constant occurrence of high pressure cells prevent precipitation with the exception of the occasional thunderstorm. Most of the precipitation occurs in the winter months. Measurements taken over the period of 1950 to 1970 show that the basin has an average temperature of 12.5° C and an average precipitation rate of 1044mm. About 62% of the annual precipitation falls in the period of September to March, with its peak in October at 16%. The spatial variations of the precipitation amount can vary within the basin (Leenheer, 2006).

## 2.2 Gully erosion

Erosion occurs when sediment loss rates exceed sediment replenishment rates in certain areas. Three types of water induced erosion exist; splash, sheet and gully erosion (Morgan & Davidson, 1986), this study will focus solely on the latter. Gully erosion represents an important soil degradation process especially in arid lands, contributing on average 50–80% of sediment production by precipitation induced erosion (Poesen et al. 2002). A distinction should be made between long term gullies and ephemeral (short time) gullies. Ephemeral U-shaped gullies are much more recent developed gullies; they are often the result of land use change. Whereas long term V-shaped gullies have often existed for extended periods of time. The latter tend to be much larger, up to one order of magnitude.

Gully erosion might have a negative impact on land use itself. Gullies allow for ground water to become runoff this significantly reduces infiltration and soil moisture; it lowers the water table in the surrounding areas leading to loss of biomass and aridification. And, gully runoff might also hamper deep ground water infiltration. However in areas of severe soil crusting the gullies are found to be water retainers and sources of ground water recharge (Poesen, 2003). These effects can be devastating for agriculture. In addition, the occurrence of gullies near roads or buildings, create a potential for collapse due to under cutting of the soil at its base. And the simple loss of area to unwanted gullies can also be a severe nuisance to the owners of the land.

The gullies of the Salagou area, the focus of this report, are long term gullies. In this chapter first the dynamics of gullies are described and the controlling factors are presented according to contemporary knowledge. Next the measurement methods which are in use today are described and prevention methods are explained in short.

### 2.2.1 Gully dynamics

Macro channel formation is a result of continued scouring; it is considered a gully when it is large enough to obstruct agriculture, whereas rills can still be filled by tillage operations according to Chaplot (2013). Other authors determine the difference between rills and gullies purely by depth. Poesen et al. (2003) describes the difference as a relationship between discharge ( $Q$ ) and width ( $W$ ), figure 7 is a graph which indicates the  $Q$ - $W$  relations for several orders of magnitudes and their corresponding geomorphology. Poesen et al. (2003) also indicates that the driving force which determines the width and depth of a gully in a homogenous soil is peak discharge.

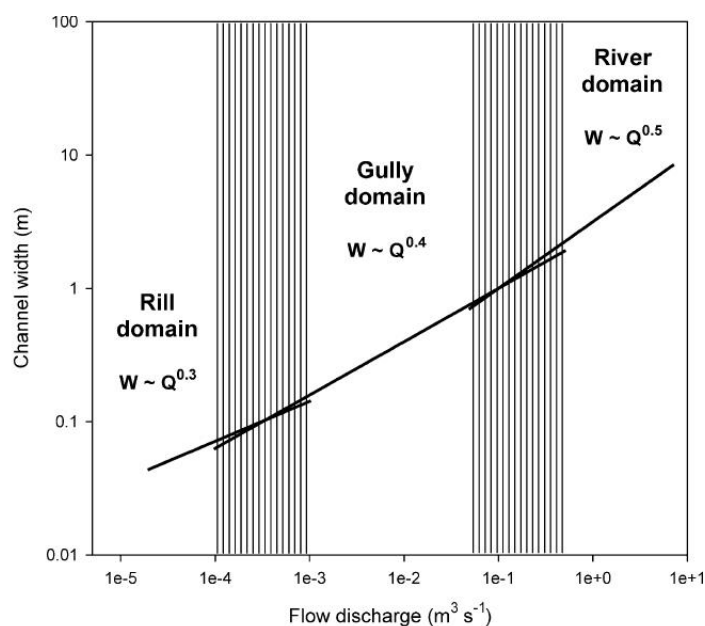


Figure 8 Width – discharge relationships, acquired from Poesen (2003), notice the change in  $b$  for different

Gullies tend to form in existing depressions in the landscape, on tectonic fault lines or anticlines, on a softer lithology or more easily erodible soil and they can also cut in to existing older geomorphologic units which had depressions. Gullies might also be created due to tunnel collapse of subsurface piping. When overland flows reach a certain velocity threshold, the soil starts to erode, scouring occurs and rills form.

Once a gully starts to form, the process is hard to reverse. The increased relief on the flanks creates higher flow speeds which causes more erosion and widening. Incision lowers the base of the gully making it more susceptible to seepage which will cause increased overland flow in the gully. Deeper gullies experience higher hydrostatic soil water pressure; this causes undercutting and increases collapse of the gully flanks. Subsurface flow of ground water called piping also tends to exit in gullies increasing overland flow and subsequent erosion. Mass wasting processes occur on the flanks of the gullies leading to landslides. Valentin (2005) has identified the following controlling factors of gully erosion: topography, soil, climate and land use. They will be described in the following sections.

### *Topographic factor*

When looking at the topographic factors one has to distinguish between the topography of the surrounding area and the topography of the gully itself. The topography of the surrounding area determines the prerequisites for gully initiation. Poesen et al. (2003) identified Hortonian overland flow to be the driving mechanism initiating gully erosion. According to Chaplot (2013) several studies have concluded that the initiation of gully formation depends on the relationship (see equation 1) between the mean slope gradient (S) and the area per unit contour length (As), which is the up slope area from which precipitation will drain into the gully. In combination they determine the flow accumulation and flow speed at a certain point. If this reached a threshold the gully formation will start to occur. Several attempts have been made to determine this threshold, the formula used is always a relation between the mean slope and the catchment; for instance Chaplot (2013) and several others have used an empirical approach. Whereas Poesen et al. (2003) used a more physical approach calculating the actual amount of pressure needed to initiate gully formation.

Equation 1:

$$\text{Threshold value} = S \times As^a \text{ (Chaplot, 2013)}$$

Chaplot (2013) shows the way in which the formula is written, the parameter a, and the threshold value still vary a lot over the different studies done in to the subject, it differs for soil conditions and land use types. So no consensus has been reached on how to quantify gully initiation. In addition, the conclusion that gully erosion is initiated by topographically controlled Hortonian flow might not be true for all areas. For instance, Bocco (1991) concluded that gully erosion is initiated by a combination of saturation overland flow and subsurface piping, during heavy precipitation events, as opposed to Hortonian overland flow.

### *Soil & lithology factor*

Soil type, and more specifically the vertical distribution of the erosion resistance of the soil horizons have a large impact on the development of ephemeral gullies (Poesen et al., 2003). The mineral- and clay- rich B-horizon often acts as a confining limiting gully development due to its higher erosion threshold. There is still little known about the properties of parent material (lithology) with respect to erosion resistance in the case of gully erosion. Chaplot (2013) concluded that the grain size of parent material did not have a large definite effect on gully on gully bank retreat.

Another major factor affecting flow accumulation and overland flow is soil crusting. Soil crusts are a thin layer on the ground surface of low permeability which hampers infiltration of precipitation and exacerbates the creation of runoff. Soil crusts tend to develop much better on gentle slopes than on steep slope this adds considerably to the runoff. This means that the flow accumulation on very gentle slopes, as low as 1% can be enough to initiate gully formation (Valentin et al., 2005). Due to soil crusting and increased flow accumulation on gentle slopes, steeper slopes do not necessarily create highest energy environments for gully erosion to commence.

### *Land use factor*

Valentin (2005) describes the effects of land use on gullies formation in great detail. Land use change often affects the generation of runoff and infiltration rates, which are important factors in gully development. Vegetation tends to hold the soil together which decreases soil erosion. In addition the roots will increase infiltration rates and the canopy will intercept precipitation. Both factors decrease overland flow. Agriculture can cause a depletion of nutrient which reduces the soil stability. In addition, cultivation can lead to increased soil crusting. Both factors exacerbate gully formation, so the occurrence of agriculture is seen as a major cause for initiating gully erosion. Deforestation significantly reduces soil cohesion and increases the possibilities for soil crusts to form. Some pastures are subject to overgrazing which destabilizes soil cohesion and allows for gully erosion to occur. Some large gullies of which the geomorphology has now become stable are found in contemporary European forest. They have been related to several phases of mostly land use but also climate change over the past 600 years, (Dotterweich et al, 2003). Next to agriculture, road construction and urban development also significantly affect gully occurrence by creating low permeability and increasing runoff (Piccarreta, 2012).

### *Climatic factor*

The driving force behind gully erosion is precipitation, which is connected to climate. During a cloud bursts infiltration capacity is quickly reached and erosion inducing runoff occurs. Semi-arid regions are often known for their few but intense precipitation events, which favor gully erosion. Climate also affects the prevalence of soil crusting, which thrive in dry periods. In addition infiltration and soil cohesion increasing vegetation types and patterns are also governed to a large extent by climatic conditions. Poesen et al. (2003) concludes that events with increasing return periods which are less intense events also yield less soil loss and subsequent gully development. Climate change and the effect which this will have on rainfall patterns will have a profound effect on gully development in the future.

### *Factors affecting the Salagou area*

Conditions in the Salagou area are a perfect storm for gully formation. The hard impermeable basalts at the top of the landscape cause precipitation to accumulate and run off the sides on the already heavily inclined slopes of the higher parts of the geomorphologic stage, in which the gullies of the third stage made their incision. The hard pelite rock of the second and third stage do not allow for much infiltration either, increasing surface runoff. Although the hard lithology does provide more resistance against erosion. Vegetation cover and soil formation on top of the basaltic plateau provides some relief however on the steep eroded slopes of the second stage this is nearly absent. Tillage mostly occurred around the gullies on the flatter areas of the second stage above the head of incision and on top of the plateau, this causes soil crusts to develop further exacerbating flow accumulation. Finally, Mediterranean climate favors bursty showers creating a lot of precipitation over a short time.

### **2.2.2 Gully erosion measurement**

Poesen et al. (2003) describes several measurement methods which are currently in use to quantify gully erosion. Most gully erosion measurements focus on the change in topography of gullies over time to compute soil loss rates. Laboratory experiments, recreating gully erosion in a controlled environment (precipitation, topography, soil) have been done; however due to the diverse conditions in which real world gully systems occur, their results are hard to link to reality.

First, some methods which do not use gully topography as its fundamental principle will be described. Next the topographic methods will be described, in which a distinction between 2D (orthomosaics) and 3D (elevation models) methods can be made.

#### *Non-topographic methods*

It is possible to use direct measurements of soil loss at the outlet of a gully, typically the lowest point in the catchment. Discharge and sediment monitoring stations are often placed at these locations (Øygarden, 2003), or sediment traps like check dams. By retrieving the volumes at certain intervals erosion rates can be calculated. One drawback of this method is that it is not possible to extrapolate which sediments came from a gully and which sediments came from the surrounding areas and have been transported by other erosion mechanisms. Finger printing of sediments using various types chemical or isotope tracers has been done (Samani et al., 2011); this revealed the difference between erosion volume of different soil layers and parent materials.

#### *Measuring gully topography*

As a desk study, historical documents, maps and paintings have been used to examine gully development (Dotterweich et al., 2003). This part will however focus on the infield methods of measuring gully topography.

As a 2D method, many studies utilize a time series of aerial photographs to reveal differences in gully outline and appearance, which can be related to gully dynamics and be used to calculate erosion rates. By creating orthomosaics, which are explained in chapter 2.3, it is possible to make accurate measurements of gully bank and gully head retreat on a horizontal plane. It is possible to overlay the outlines of the gully borders to quantify differences over time.

Large scale studies into the occurrence of gullies have been done using satellite based remote sensing methods. For instance Ibokwe et al. (2008) have used data from several satellites to compute land use, soil, slope and vegetation maps. By combining these, the susceptibility to gully erosion was calculated. However due to the coarse resolutions of satellite imagery their accuracy is inadequate.

To create 3D representations of gully systems some basic and some advanced methods can be used. Advanced methods use innovative technical techniques to create comprehensive DEMs whereas basic methods provide much coarser DEMs. Some Basic methods are described by Poesen et al. (2003), Poesen (2011) commented on the needed proliferation of advanced DEM creation methods for gully erosion monitoring. First some of the basic methods in existence will be discussed, then the more advanced techniques and finally the technique used in this study will be elaborated upon.

The retreat of a gully banks or heads can be measured by placing markers, which are used as reference points inside the gully and measuring the distance between the marker and the edge of the gully at certain intervals. Accurate slope descriptions of gully walls have been made using protractors; making several of these descriptions at different times also provides the ability to gain a better insight in to gully dynamics and soil loss rates. Bonnet et al. (2001) used DGPS surveying to create DEMs of gully systems, measuring the thalweg and the crests of the gullies. By connecting the crests it is possible to recreate the previous geomorphologic stage as can be seen in figure 9. This data could also be used to create long term gully erosion volume estimates by subtraction, as is the focus of this study.

More advanced methods include: Interferometric synthetic aperture radar (InSAR), Light Detection And Ranging (LiDAR) and photometry. The former two are active remote sensing methods which are considerably more expensive than photometry, the technique used for this project. LiDAR has the large added benefit that it can detect the surface underneath vegetation; this poses a large problem for photometry methods. Perroy et al. (2010) compared ground based the LiDAR wit airborne LiDAR for DEM creation on gullies. They concluded that although the ground based LiDAR (TLS) is considerably more accurate than the airborne method it suffers from a lot of errors due to obscurities related to its low angle of incidence. This makes TLS methods a considerably less viable option.

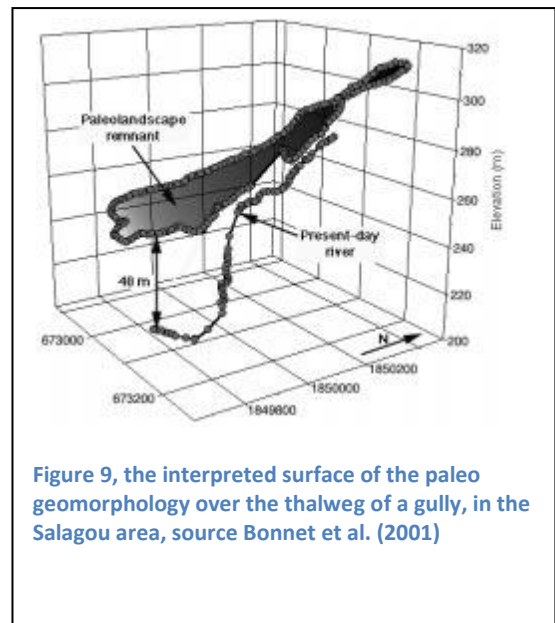


Figure 9, the interpreted surface of the paleo geomorphology over the thalweg of a gully, in the Salagou area, source Bonnet et al. (2001)



## Photometry

The photometry method allows for DEMs to be created from overlapping photographs; it is described extensively in chapter 2.4. Photometry has the added benefit that it can be used on older existing aerial photographs to compute historic DEMs, which is crucial if you want to analyze time series of DEMs.

Picaretta et al. (2012) used comparison of three different DEMs taken at the same location in Southern Italy, in the years 1949, 1986 and 2000 to compute total erosion losses by method of subtraction. In addition land use change and gully borders were monitored using aerial orthophotos of around the same time periods. Pluviometric data revealed a decrease in annual precipitation and rainfall intensity. However there was an increase in soil loss over the same period. It was concluded that the land use change had a bigger effect on sediment change than climatic change.

Marzloff & Poesen (2009) also used DEM comparison to reveal gully dynamics; their results are given in figure 10 and 11, they show the volumetric differences due to gully formation over a four year period. Some places of the gullies show an increase in elevation, this can be attributed to mass wasting processes and infilling. This method of subtracting photometric DEMs is the most suited for the task of calculating gully erosion due to its high accuracy, comprehensive DEMs which it yields and comparatively low cost.

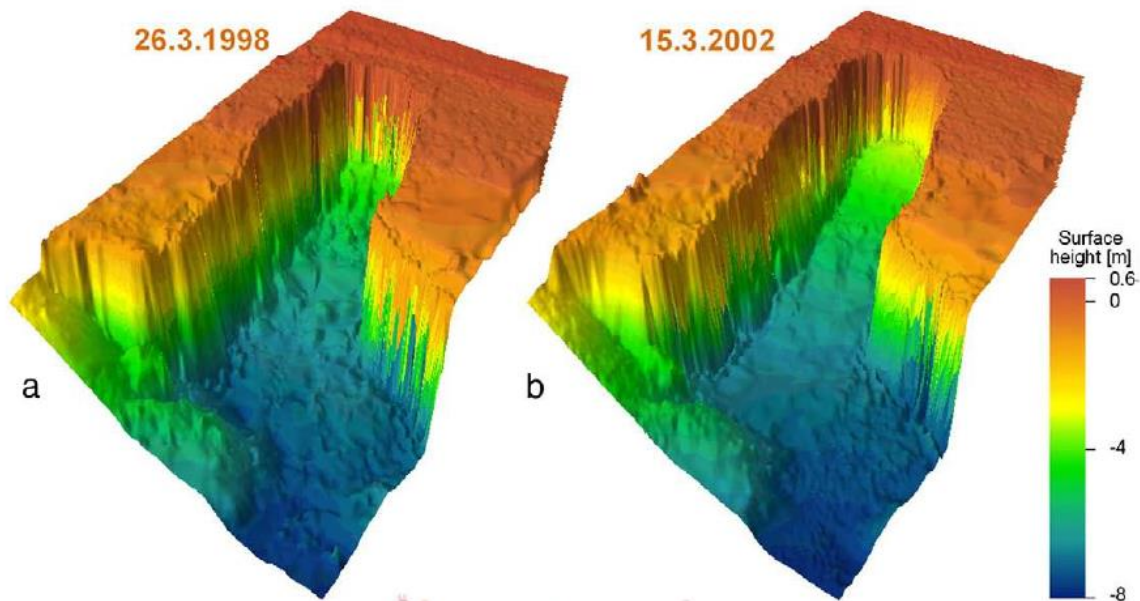


Figure 10, two DEMs of the same location taken 4 years apart by Marzloff & Poesen (2009)

2002 – 1998

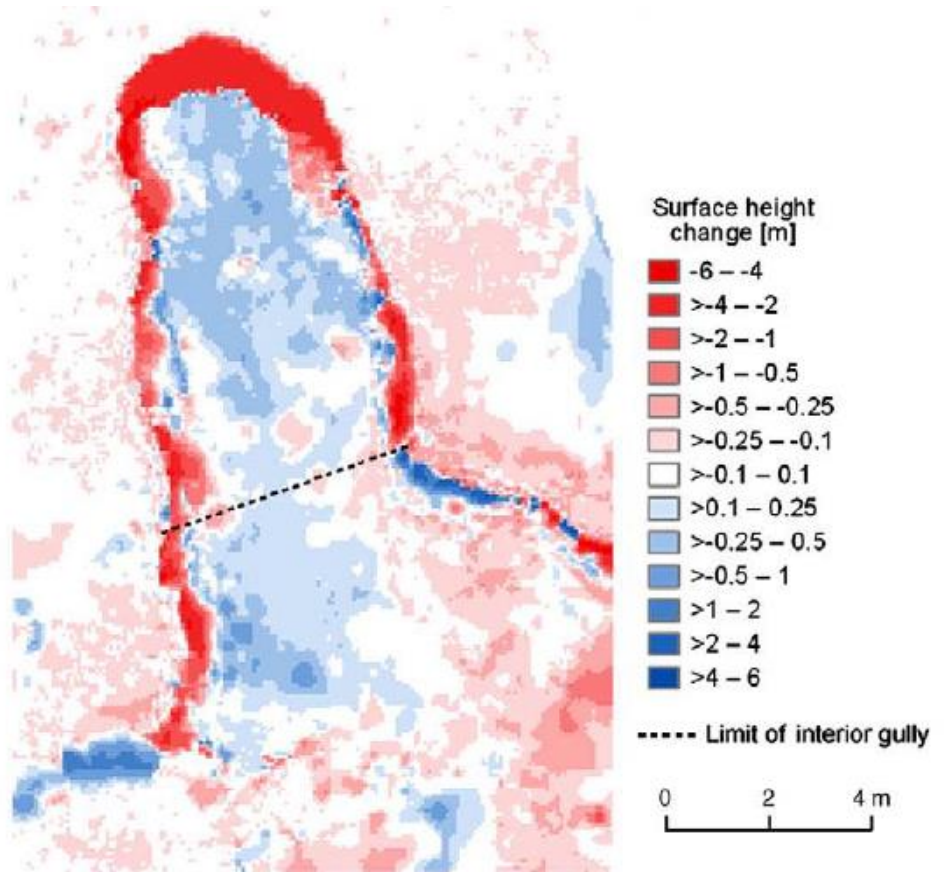


Figure 11, DEM difference map by Marzolf & Poesen (2009)

## 2.3 Unmanned Aerial Vehicles

### 2.3.1 Context

#### *Nomenclature*

Most sources utilize the word UAV (unmanned aerial vehicle) however sometimes UAS (unmanned aircraft system) or UAVS (unmanned aircraft vehicle system) or RPAS (remotely piloted aircraft system) are used (Watts et al., 2012); the term drone is often used colloquially. RPV (remotely piloted vehicle) is an old term used by the US military. The terms UAS and UAVS typically also include the ground control station. This thesis will only use the designation UAV. Although a kite or a balloon is technically an UAV, contemporary use of the term applies to automated remote controlled systems.

#### *A military history*

The earliest notion of UAVs stems from the end of the 19<sup>th</sup> century. Early experiments consisted of putting cameras on balloons, kites, rockets and even pigeons (Newhall, 1969), see figure 12. Nikola Tesla philosophized about the occurrence of unmanned combat vehicles in future wars as early as 1915. And the first attempts at creating flying bombs stem from world war one. In world war two both the Nazis and the allies experimented with UAVs for reconnaissance and the allies used them for target practice. The first combat use of UAVs occurred in the Yom Kippur war where UAVs were used by Israel to map the Syrian surface to air missile systems which subsequently shot down the drones allowing for the real fighter jets to take out the defenses while they reloaded. Since then the United States military spearheaded the development and use of UAVs to keep their edge over their opponents; the last two decades especially have seen rapid advances. In the military, UAVs are used for tasks which are considered 'dull, dirty and dangerous': dull refers to lengthy reconnaissance missions, dirty refers to chemical tests and radiation probes and dangerous concerns missions with a low survival chance (Tice, 1990). Today drones are a commonplace occurrence on modern battlefields and have the ability to take out targets themselves. At the moment in the United States air force UAVs outnumber regular planes two to one.

Scientific use of UAV typically lagged behind military applications. Unmanned balloons were used to take photographs of archeological sites since the early 1970s; while the first fixed wing and rotary wing solutions occurred in 1979 and 1980 respectively. Early developments were plagued by sensor errors in both exterior positioning and image quality (Eisenbeiss, 2009).

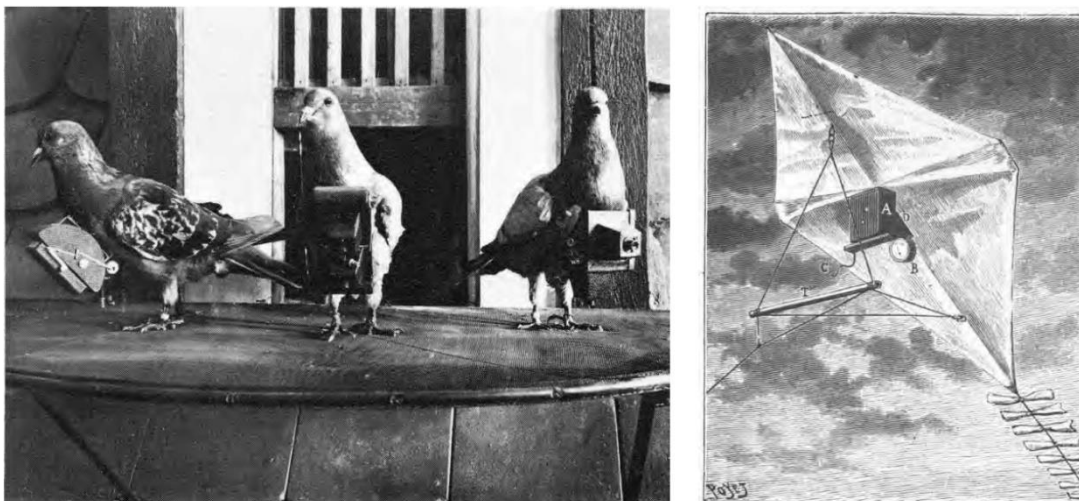


Figure 12, pigeons and kites with timed cameras attached were the first UAVs (Newhall, 1969)

### 2.3.2 An unmanned aerial system

The system discussed here is geared towards small UAV use in the field for scientific purposes. The components may vary for other types of UAVs and applications. But the general principle is the same. The main components of the system are a ground control station, a pilot and the UAV itself. A computer is used for pre-flight planning and post-flight processing. The latter will be described extensively in chapter 2.4. Much of the information provided here is the result of experiences gained at preliminary runs with UAVs done in the Netherlands. In addition the website [www.hoogtezicht.nl](http://www.hoogtezicht.nl) was used as an information source (a Dutch UAV enthusiast information site).

#### *Ground control station*

An extensive description of what a ground station should include can be found in Hong et al. (2008). The ground control station usually consists of a laptop, a data link, and a pilot with a remote control. Ground control station or GCS in short can also refer to the type flight control software used. The data link consists of an antenna which is connected to the laptop. The laptop will run the GCS to monitor the UAV's status in flight. The internal navigation system (INS) constantly relays flight information to the GCS. In addition sensor data is also relayed and can be used to determine its accuracy, usefulness and to bring to light any possible errors. In the case of automated flight the waypoints are pre-planned in the GCS and can be changed on demand in flight. Some UAVs will have dedicated software which can be accessed upon purchase, like eMotion 2.0 which comes with a swinglet drone. Some Autopilot add-ons also have dedicated software to them, like APM 2.5 which comes with the ArduPilot. There are also open source options available, like WeGCS.

Although many UAVs have the capability to fly autonomously, an experienced UAV pilot is still required in case of an emergency. The range of the remote control determines the area in which the UAV can fly, this is dependent on the type of transmitter and receiver. For a pilot to fly a drone beyond the line of sight a video link upgrade can be used providing that the drone has an onboard camera. To determine the strength of the connection a range check is usually done pre-flight. The pilot checks the reception on the ground at a certain distance with a weaker signal, this can then be related to a larger distance at full transmission strength in the air.

## *The UAV*

The components inside the UAV are: a motor, a data link, a sensor, a RC receiver, a battery, the chassis, an INS, and optionally an autopilot and stabilizer. The chassis's aerodynamic shape provides lift and it holds the other equipment. The INS will be described in the next section, as it is of great importance for image processing. The battery is the UAVs power source, its lifetime determines the airtime of the vehicle. The motor is usually electric, however in larger UAV internal combustion engines are sometimes fitted for more power. The data link transmits and receives data, it is connected with the ground control station; While the RC receiver can receive commands from the remote control. A stabilizer is connected to the INS and it is used to assist the pilot in flight. An auto pilot chip guides the UAV in the case of autonomous flight; it typically includes a stabilizer as well.

## *Internal navigation system*

The internal navigation system (INS), also called the inertial measurement unit (IMU), usually consists of a combination of GPS receivers, gyroscopes and accelerometers, and in most cases a barometer and a magnetometer. Angular accelerometers measure the acceleration of the aspect displacement along the three axis of the aircraft. Pitch is angular displacement along the x-axis, roll along the y-axis and yaw along the z-axis, see figure 13 for a schematic overview. Especially changes in pitch and roll can greatly affect the obliqueness and therefore quality of images. The gyroscopes are used to indicate the angular reference frame for the accelerometers. In addition linear accelerometers measure the linear accelerations in x, y and z direction with the vehicle as reference frame. The vertical accelerometer(z-axis) has been adjusted to negate the effect of gravity. A magnetometer measures the direction of the earth's magnetic field and therefore the compass heading of the UAV, it is also used to calibrate the gyroscopes. A barometer is used to measure atmospheric pressure which can be related to altitude. A GPS receiver calculates its location in longitude and latitude as well as height. The resulting position is accurate within several meters, which depending on the application might be sufficient for geocoding images, however for this study it is not.

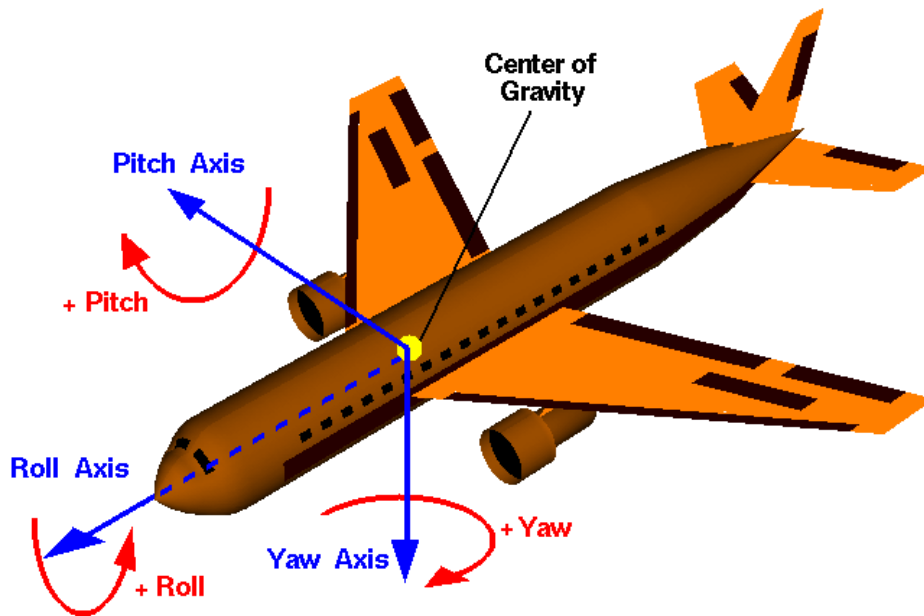


Figure 13, a schematic over view of pitch, yaw and roll

### 2.3.3 Types, applications and status of UAVs

#### *Types of UAV*

These days a wide variety of UAV types exist for an array of different applications for: military, commercial and private use. Watts et al. (2012) gives an overview of the different UAV platforms which are in use today. UAV types range from miniature air vehicles the size of small birds to high altitude long endurance vehicles which are the size of conventional aircraft, they can stay up in the air for extended periods of time. A special type of UAV are the vertical take-off and landing vehicles (VTOL), which use rotors instead of wings, these can provide a steady platform to take measurements. There are two classification methods. They are either classified according to flight altitude and endurance (Watts et al., 2012), as is explained in figure 14. Or they classified according to power use, as is proposed by Eisenbeiss (2009), see table 2. The second classification is better suited to small scale UAVs, as it also includes balloons and kites. Whereas, the former is better suited to distinguish larger UAVs.

# UAV Nomenclature Designations

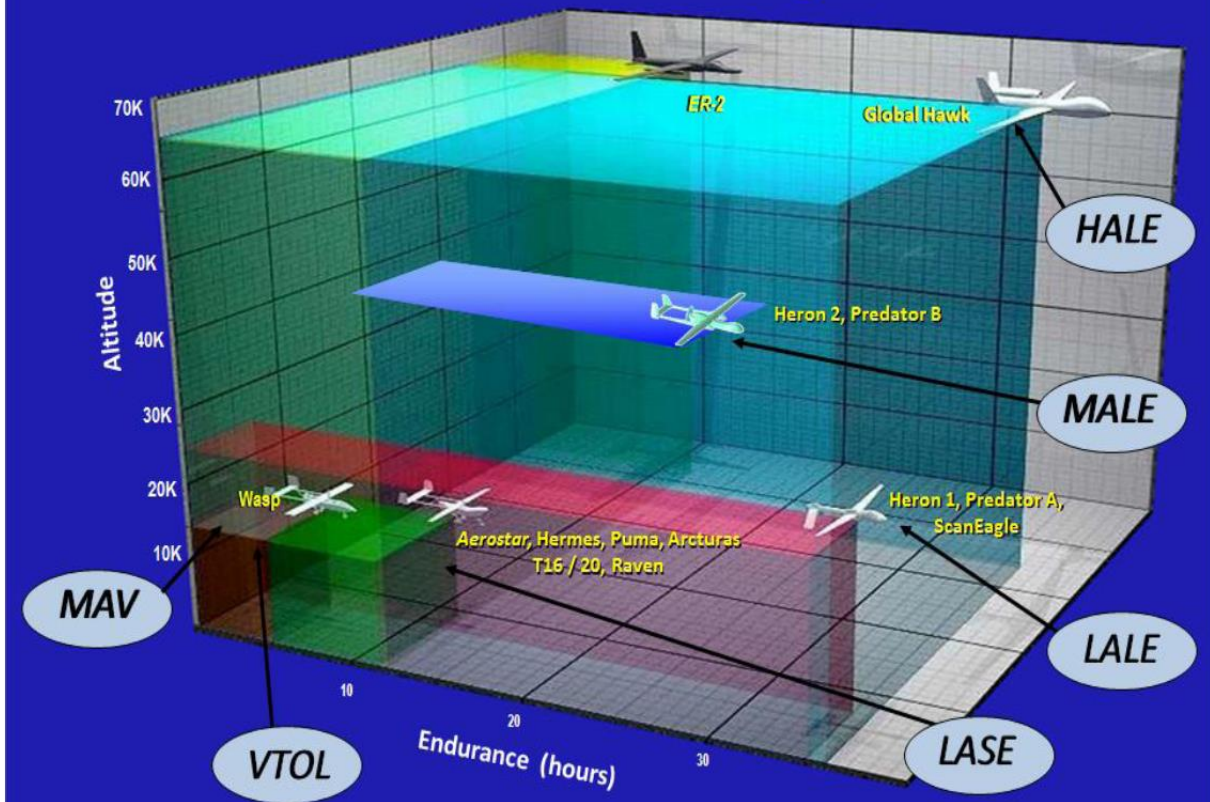


Figure 14, UAV classification according to Watts et al. (2012). MAV: miniature or micro aerial vehicle. VTOL: vertical take-off and landing i.e. rotary wing. LASE: low altitude short endurance. LALE: low altitude long endurance. MALE: mid altitude long endurance. HALE: high altitude long endurance.

Table 2, UAV classification according to Eisenbeiss (2009). It includes kites and balloons and the various types of rotary wings, however the powered fixed wing aircraft are lumped together.

	Lighter than air	Heavier than air		
		<i>Flexible wing</i>	<i>Fixed wing</i>	<i>Rotary wing</i>
<b>Unpowered</b>	Balloon	Hang glider	Gliders	Rotor-kite
		Paraglider		
		Kites		
<b>Powered</b>	Airship	Paraglider	Propeller	Single rotors
			Jet engines	Coaxial
				Quadrotors
				Multi-rotors

### Pros and cons

Eisenbeiss (2009) describes the advantages and limitations of the uses of small UAVs; A quick overview of these pros and cons of UAVs is given in table 3.

UAVs allow for the exploration of new scientific fields, see appendix A for an overview of the applications. They can investigate potentially hazardous areas where men or other remote sensing device cannot go, such as: landslides, hurricanes, volcanoes and other natural disaster sites. In addition they are able to fly at very low altitudes, this yields a higher image resolution than conventional airborne or satellite imagery. And, their ease of use and operational flexibility allow for high temporal resolutions when investigating dynamic processes. The commercial market of UAVs focuses on small low cost systems, this makes them comparatively very cheap, which is a major advantage. Due to the low flight height, UAV imagery is not affected by clouds and drizzly weather, this increases their operational capability. Obviously UAVs do not require onboard pilots, this significantly reduces space in the vehicle and costs for wages. When used to create 3D landscape models they are considerably less labor intensive and costly than other methods such as laser scanning or airborne LiDAR. UAVs are especially well suited for application on a comparatively small scale which requires a high resolution.

One of the major drawbacks of a UAV is the fact that it can only carry small and light payloads. This translates into light weight sensors which tend to be less accurate and have less capabilities. Often consumer grade cameras are used which require many images to be taken to cover an area. The smaller payload also translates to smaller less accurate internal navigation system (INS) which, in combination with the high image resolution of the final product, means that often more accurate ground observations are needed for processing. In addition the absence of an onboard pilot is both a blessing and a curse; a UAV does not have the capability to sense objects in its surroundings or know when something goes wrong. In the case of autonomous flight a UAV pilot should always be present to step in in case of an emergency. Due to the low flying height and light weight of the UAV, atmospheric differences have a large effect on the orientation of the vehicle; in other words they can be wobbly in flight. This means the resulting images should be assessed for large differences in pitch, yaw and roll. Also, UAVs often have a small reach which is limited to either the pilots line of sight or the range of the radio control transmitter; this can make covering large areas or areas with high relief a tedious task.

Table 3, Pros and Cons of UAV use.

Pros	Cons
Access to hazardous areas	Small operational distance
High image resolution	Small payloads (low level sensors)
Temporal flexibility	Ground pilot still needed
Low costs	Inaccurate INS
No clouds	Wobbly



## *Contemporary status of UAVs*

UAV-based remote sensing is an area of remote sensing which is undergoing rapid developments and is not yet near consolidation (Evearts, 2008). Many research groups around the globe have benefited from UAV's low cost and wide applicability. In addition UAVs have opened the way for many new users of remote sensing methods. Miniaturization of sensors, batteries and motors will continue to increase the UAVs versatility in the future. One major upcoming development which can improve on the method of image processing is the possibility of putting more accurate RTK DGPS on a UAV, which might eliminate the need for ground control points (see chapter 3 for more information on ground control points). In addition post-processing of differential GPS data can be done taking part of the computation process away from the INS, which only measures the raw GPS data, making it both lighter and cheaper (Bláha et al., 2011).

Civil airspace and aircraft regulations have not managed to keep up with the rapid developments and increase of private use of UAVs. Due to the absence of a human pilot and the fact that UAVs are typically not made to sense objects in the surrounding airspace most countries forbid UAVs from entering civil airspace. As of June 2013 the Dutch ministry of defense suspended the need to have a permit for aerial photography (Hoogtezicht, 2013). In addition there are currently conceptual laws which are not yet in force which distinguish between amateur recreational use of UAVs and professional use, both commercial and governmental. The DeSIRE project a joint project of the European Space Agency and the European Defense Agency investigates the possibility of allowing UAVs in civilian airspace using satellite based technology (DeSIRE, 2013). Another complication delaying lawmakers are privacy concerns stemming from the fact that small UAV allow for an unprecedented ability monitor people.

## **2.4 Photometry**

### **2.4.1 Context**

From a flight with a UAV, a set of single, often blurred and moved images are acquired. Structure from motion is the process, consisting of a set of computer algorithms, which utilizes these images to recreate the 3D environment.

### *Structure from motion*

Multi-view Stereopsis (MVS) is the computer process in which multiple overlapping photographs taken at different angles are used to derive a 3D model (Furakawa & Ponce, 2010). Structure from motion (SfM) is the process of applying 3D model building techniques to data acquired in 2D from the same camera on a moving platform. These two terms are sometimes used to indicate the same process which is described in this chapter. MVS was developed focusing on single objects using multiple stationary cameras, however the MVS algorithms can be used for SfM (Zisserman, 2004). The process makes use of computer vision (CV) as it is known in the field of robotics. The process can be compared to the way in which humans see 3D even though the images hitting our retinas are in 2D, the computer is in this case the brain which does the conversion. 3D representations of a scene using UAV based stereoscopy shall hence further be referred to as UAV photometry.

Although SfM and MVS techniques were not developed for environmental surveying they are well suited for the purpose. Since geomorphologic features are three dimensional features visible at the earth surface, SfM techniques used on aerial photography can yield 3D representations of the land surface (Eisenbeiss, 2009). 3D structures acquired from UAV Photometry can be interpolated to

a digital surface model (DSM) which can have a wide range of applications, which will be discussed in section 2.4.4. Another product of UAV photometry which can be acquired from a set of overlapping Aerial photographs is an orthorectified mosaic. Since UAVs can fly closer to the ground than conventional aircrafts a very high resolution can be achieved for aerial photos taken from that platform. However due to this comparatively small distance between the sensor and the scene, relief in the scene will distort the photograph especially at the edges.

### *Development of computer vision*

The recent decades have seen significant ongoing and increasing developments in robotics and computer vision. The development of automated image matching which used to be done manually has significantly reduced processing times. Goesele et al. (2007) have shown that it is possible to create 3D point clouds out of tourist made photographs acquired from the internet. Even though the photos were taken at different times of day and under different weather conditions they still yield decent results. And SfM feature matching techniques are currently being developed which tailor especially to movie clips (Ramachandran, 2011). Some of these techniques are already in use for cinematography by programs like Adobe After Effects to which can edit movie clips and add special effects.

### *Contemporary research*

Several research groups are currently focusing on the development of UAV photometry, some prominent groups which have their literature used for this report are: the UAV-group at the ETH in Zurich (Eisenbeiss, 2009) and the TerraLuma project of the University of Tasmania (Harwin & Lucieer, 2012). A major European conference called UAV-g into the subject was held in 2011 in Zurich, many of its proceedings are used as references in this report. The next large conference was held in September 2013 in Rostock, Germany (<http://www.uav-g.org/>).

## **2.4.2 Image processing**

### *The use of ground control points*

When an accurate DEM is desired a set of images is not the only data which is required. Eisenbeiss (2009) has stressed the use of ground control points (GCPs) to improve the accuracy of UAV photometry products. Low cost UAVs with limited lift capabilities tend to carry insufficiently accurate INS, see chapter 2.2. In addition the low flight altitude of the UAV yields very high resolution images. This means that the exterior orientation data is not accurate enough to create a DEM with a satisfying resolution and error margin for some applications. By using ground control points or GCPs for short it is possible to significantly reduce the error of the DEM and increase the accuracy of georeferencing. A GCP is a ground measurement acquired using DGPS, the location of which is marked so that it stands out in images. During image processing some software package allow for the identification of GCPs, this process is either completely manual or computer assisted. Increases in accuracy of light weight INS and sensors might make the use of GCPs obsolete in the future. Some ground control points are used to test the accuracy of the DEM with respect to a real world coordinate system. These reference points are not used in the initial computation but are used as a ground truth.

### *3D point cloud extraction*

Various programs (see table 4) can be used for processing overlapping images to create a 3D-model, however they all use the same approach. A schematic overview of the image processing used by Harwin and Lucieer in 2012 is given in figure 15. They took a raw approach using open source software. Most proprietary software will use the same structure algorithms which are integrated in the shell. These basic steps of the process are explained below (Aber et al., 2010):

1. The construction of a 3D image relies on the extraction of corresponding points in multiple images, these are typically corners and shadows, this process called feature matching. The latest development for this is a method called SIFT, a feature matching algorithm which identifies regions rather than points. Other methods include Gradient Location and Orientation Histogram (GLOH), Speeded Up Robust Features (SURF), LDAHash and Principal Component Analysis (PCA)SIFT. SIFT is thought to be the most accurate (Harwin & Lucieer, 2012). Feature matching might experience difficulties in areas of dense vegetation.
2. After feature matching a bundle block adjustment is applied. This is an algorithm which computes the external orientation of the camera within the image space, which is its relative position and angle compared to the points acquired using feature matching. In addition it describes the 3D structure of the scene simultaneously (Hartley & Zisserman, 2004). It is an optimal algorithm, which means that the error of the computed parameters is minimized by a cost function.
3. The next step in MVS is to increase the density of the point cloud. A wide variety of algorithms exists for this purpose, the most well-known are Patched based multi-view stereo (PMVS2) and Clustering views for multi-view stereo (CMVS), they both use a match and expand filter to the original feature matched points. Over a hundred algorithms for MVS are compared by Seitz et al. (2006). which concludes PMVS2 to be the best; however this has not been tested for the specific purpose of creating DSMs. Depending on the software used it is often possible to use GCPs to make the computation more accurate.
4. The next step is to change the point cloud data from an internal image coordinate system to a real world system, like the UTM based WGS84. This is done using a Helmert transformation This can be done in either a direct or an indirect manner. The direct manner uses flight data from the UAV's internal navigation system (INS) to compute the transformation. The indirect manner uses a ground control points (GCPs) acquired using DGPS as a reference frame. The latter method typically yields a more accurate result (Turner et al., 2012). See figure 16 for an abstract presentation of the Helmert transformation.

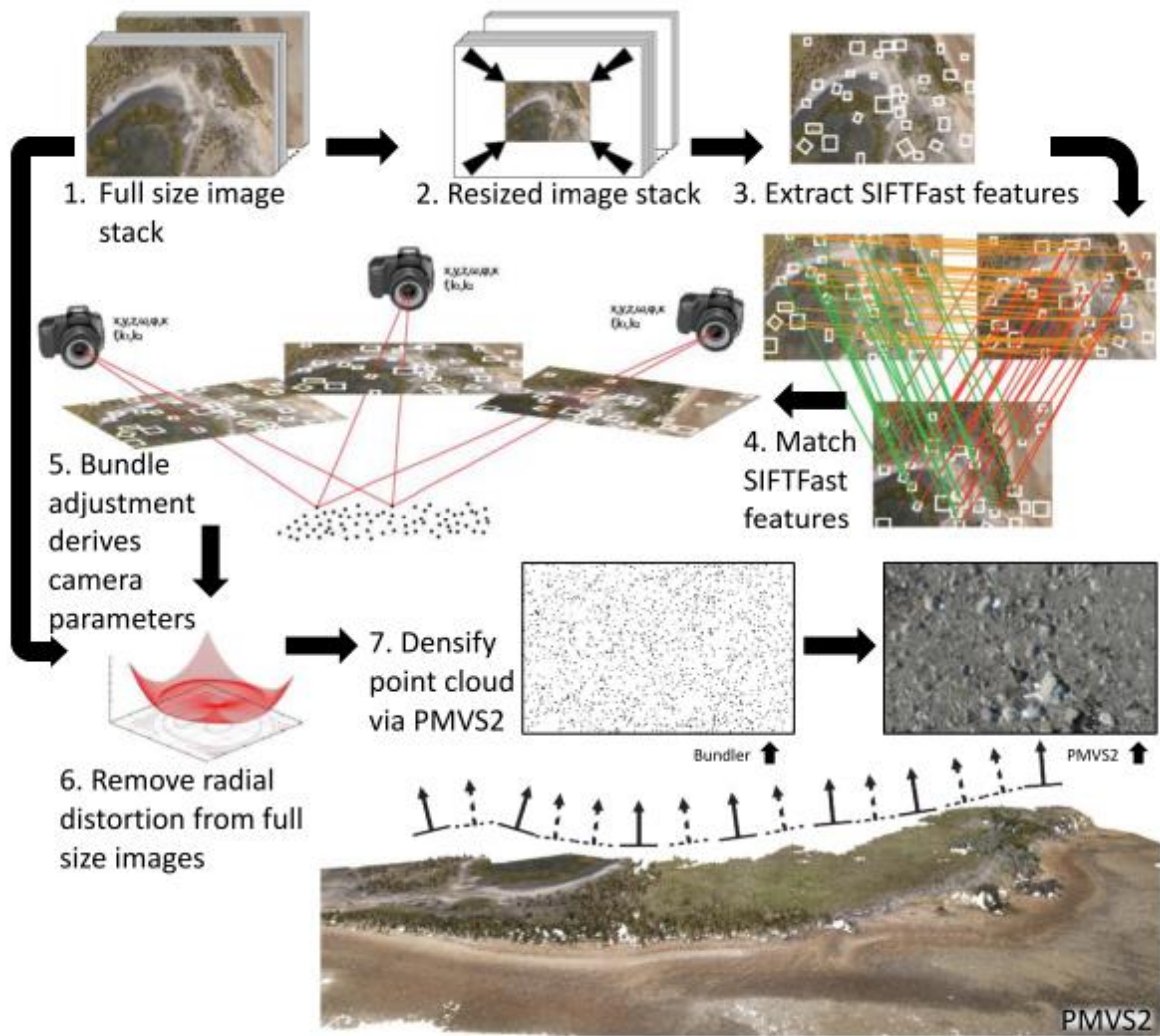


Figure 15, flowchart of the 3D-point cloud extraction process (Harwin & Lucieer, 2012). Note that the image is not yet georeferenced according to the helmert transformation.

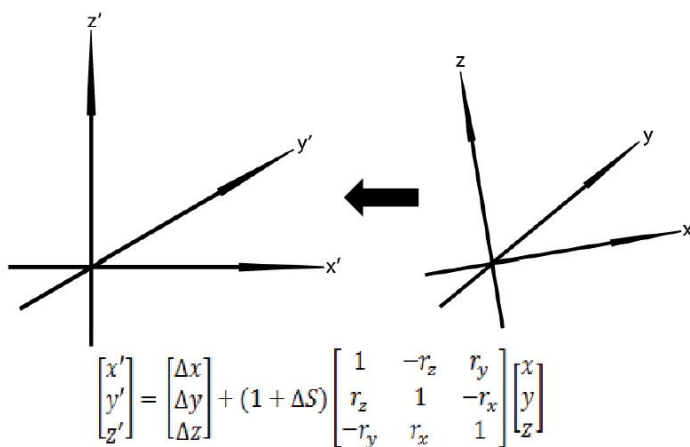


Figure 16 Schematic overview of a Helmert transformation, which is used for georeferencing.

### Erratics and errors

When computing the bundle block adjustment or when using a multi-view stereo algorithm the resulting point cloud should always be checked for erratics. Erratics can be the result of several errors. Most conventional camera lenses have a bulge effect towards the edges, this can result in false placement of 3D points. The edge effect occurs on the side of the mosaic and is the result of insufficient data at those locations.

Marzluff & Poesen (2009) looked into the possible source of error which are found in the scene of a gully system, their results are summarized in figure 17. In this figure the shaded area (A) is the result of shade in the scene which obscures underlying textures hampering the process. In the DEM it will show up as a more gentle slope than it is in reality. Shadowing can also occur due to the location of the camera position and angle with respect to the part of the scene. The steep drop (B) is often smoothed in a DEM due to a lack of 3D points along the edges. Overhanging is typical for U shaped gullies but not so much for V-shaped gullies, more on gullies in chapter 2.4. Most DEM interpolations used in surveying are actually 2.5D, meaning they will only allow one elevation value for every XY coordinate. As can be seen in figure 17, this creates a zigzag pattern in the DEM. Finally vegetation is a major source of error, the image matching process does not distinguish between plants and the earth surface. The result is a fragmented array of 3D points which do not represent a smooth surface but rather some branches, leaves and parts of the underlying soil.

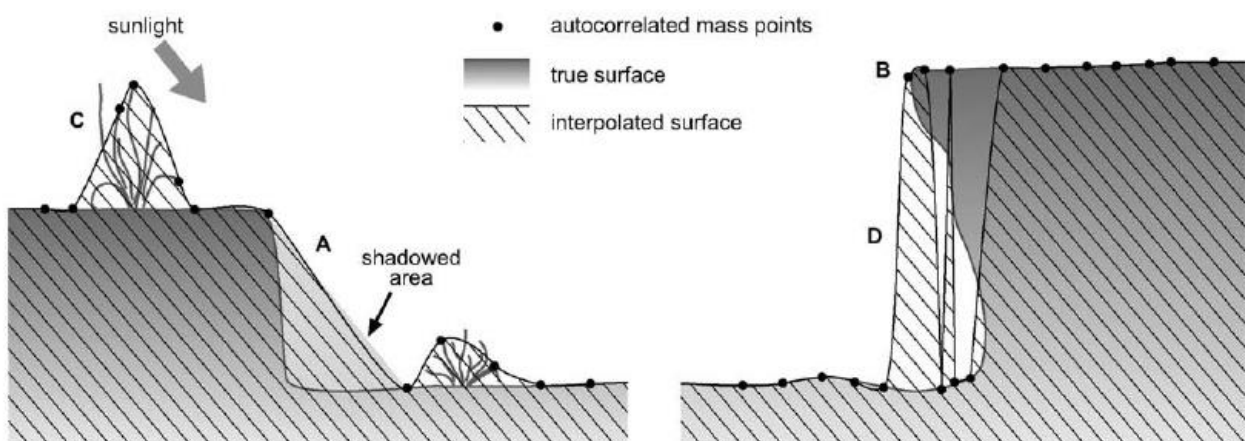


Figure 17, Sources of scene errors in photometry. (Marzluff & Poesen 2009)

### DEM generation

The resulting 3D point cloud can be used for DEM interpolation methods to fill in the gaps and create a more visual representation of the landscape. The density of the point cloud determines the accuracy of the DSM. There are several interpolation methods which might be used, the most common of which are explained below; they each have their own advantages and disadvantages. A triangular irregular network (TIN) is made using Delaunay triangulation and yields a vector map featuring many triangles. Other DEM operations typically yield raster maps. Inverse distance weighting (IDW) is a neighborhood operation applied to each 3D point. Spline, a type of radial basis function, fits a polynomial function along the 3D points to calculate the points in between the known values. Kriging takes a stochastic approach to the spline method and also yields raster representations of error margins (Burrough, 1998).

### 2.3.3 Available software

Many software packages are available. While some studies have attempted to compare some of the software packages a complete comparison of all available options has not yet been done. Some open source and freeware packages exist like Bundler, ARC3D and PMVS2. Other proprietary and commercial software packages exist like: Trimble's Inpho, Microsoft Photosynth, Erdas Leica photogram studio (LPS), Agisoft Photoscan and Geomatica by PCI Geomatics. Some software package like Pix4D are cloud-based, which allows the producer to charge per square meter of surveyed land, this can become quite expensive.

Neitzel and Klonowski (2011) did a software comparison in on several packages using the CloudCompare software. They compared Microsoft photosynth, ARC3D, Bundler, PMVS2 and Agisoft photoscan. Photoscan and a combination of Bundler and PMVS2 were found to be the best applications which produced the most complete coverage and highest amounts of points. Bundler is an open source program which focuses on the bundle block adjustment, it is especially suited to images acquired from low grade consumer cameras whose interior orientation is not known, its outcomes are used as input for PMVS2, a MVS algorithm which densifies the point cloud, also open source. In the positional accuracy of the end product Agisoft photoscan was found out to be superior while the elevation accuracy of PMVS2 was superior by a small margin, while Photoscan appeared to create a small bulging effect, see table 3 for details. Gerke (2012) compared LPS, Pix4D and 123D Catch. It was concluded that Pix4D was preferred to process UAV images since 123D catch did not allow for georeferencing and LPS was very labor intensive. Aber et al. (2010) evaluated a large number of image processing software and their capabilities and feature. The results of which are shown in table 4. Note that the list dates from 2010 and software updates might have added features to some of the software. The software subdivided in to several groups, most notably: GIS-software, remote sensing software and digital photometry software.

Table 4 comparison of software packages for image processing. Acquired from Aber et al. (2010)

SFAP image processing	Simple image-viewing software	Camera software	Professional image-editing software	GIS software	Remote sensing software	Digital photogrammetry software
Import of camera-specific image formats	○	●	○	—	—	—
Camera-specific image enhancements *	—	●	○	—	—	—
Radiometric enhancements	●	●	●	○	●	●
Image scaling / resolution change	●	●	●	●	●	○
Image rectification by GCPs	—	—	—	○	●	○
Image ortho-rectification	—	—	—	—	○ +	●
Combination with GIS vector data	—	—	—	●	○	○
Map layout	—	—	—	●	●	○
Image classification	—	—	○	○ +	●	—
Vector object extraction	—	—	○	○ +	○ +	○ +
Stereoscopic viewing	—	—	—	○ +	○ +	●
3D analysis / DEM extraction	—	—	—	—	—	●
Software examples	Ifan View	All digital camera brands	Adobe Photoshop, Adobe Lightroom, NIH image, GIMP	ESRI ArcGIS, GRASS, Quantum GIS, Intergraph GeoMedia	ERDAS Imagine, IDRISI, ENVI, GRASS, PCI Geomatica	Leica Photogrammetry Suite, SocetSet, VirtuoZo, LISA, PhotoModeler
— Not available		○ Sometimes, indirectly or partly available		○ + Usually available as an add-on module		● Available

### 2.3.2 Accuracy analysis

Various approaches exist for assessing the quality of UAV photometry products: empirical, comparison and internal error propagation. Most studies, this one included, take the empirical approach; they use DGPS or total station which have an accuracy of several centimeters, to create a sparse point cloud of reference points which are considered ground truth. The errors are calculated by taking the root mean square of the differences in elevation at the locations of the test points. To determine the horizontal error of a model reference points are compared to their markers on the orthomosaic. This section will show the accuracy analysis elevation models created by studies comparable to this one.

In a study done by Harwin & Lucieer (2012), over 300 UAV images were taken at an altitude of 30-50 meters with an overlap of 70-95% of an area with low relief; this meant that many images were discarded to reduce processing times. The study itself has used both total station and RTK GPS survey methods to calculate the GCPs used for the Helmert transformation. It concluded that the number of GCPs used to perform the Helmert transformation significantly impacted the accuracy of the 3D point cloud.

The direction of the residual errors at the GCPs are also represented in a GIS environment using Eonfusion. It shows that large horizontal errors can be found near the edges of the scene and vertical errors in places with high relief. Flat surfaces are found to be quite smooth exhibiting only very small errors. The article also stresses the need for clear GCPs with easy identifiable centers. It advises that GCPs should be distributed evenly at a distance of about one fifth of the flying height. And in steep areas the GCPs should be closer together.

Hugenholtz et al. (2013) did an accuracy assessment of a UAV photometry project. They created a DTM using 140 images and 25 GCPs. To determine the accuracy 99 reference points were taken using DGPS, in addition the study area was also surveyed using ground based LiDAR (laser scanning). The vertical RMSE of the UAV DTM was 0.29 m, the same as the RMSE of the LiDAR DTM. The median differences with the reference points for both methods were 0.07 and 0.03 respectively; this indicates that the LiDAR has more outliers. Another interesting result was the fact that for the UAV DTM the vertical differences were positive 72% of the time.

Neitzel & Klonawski (2011) made 3D point clouds of parking lots using 99 images taken at a flight altitude of 50 meters and they used 6 GCPs. They used two software packages to compute the point clouds. The errors were computed using an unspecified amount of reference points. The results of which are given in table 5. The elevation errors are very small, this is probably the result of the smooth flat easy to measure surface of the parking lot. The -25mm elevation difference within the scope of the GCPs appears to a common error in Photoscan, it is said to be the result of a bulging effect at the center which is part of the software.

Table 5 the results of Neitzel & Klonawski (2011), a comparison of Agisoft Photoscan and PMVS2

	Mean positional error (whole area)	Mean positional error (within GCPs)	Mean elevation error(whole area)	Mean elevation error (within GCPs)
PMVS2	235 mm	136 mm	5 mm	2 mm
Photoscan	256 mm	56 mm	-5 mm	-25 mm



### 2.3.4 Applications

Recent developments in UAV photometry allow for geomorphological changes to be measured at a sub-decimeter level (Harwin & Lucieer, 2012). Coupled with the temporal flexibility of image acquisition it allows us to determine the rates of geomorphological processes. This can be done for the purpose of scientific interest but also to assess the risks of natural hazards. Due to its low cost and flexible approach UAV photometry has the potential to replace ground based surveying methods in the near future (Neitzel & Klonawski, 2011). This could revolutionize workflow of many construction projects in civil engineering which require accurate elevation models. There is a proliferation of projects which utilize UAV photometry, of which some examples will be discussed here.

Currently de Jong and Immerzeel from Utrecht University are using UAV photometry to gain a better insight into glacier dynamics and relate that to climate change. Understanding seasonal glacial dynamics and quantifying glacial retreat can greatly benefit our understanding of climate change in mountainous areas. A time series of DTMs are great way to highlight vertical retreat which although less visible has a bigger impact than horizontal retreat (Immerzeel et al., 2014)

In a study done by Niethamer et al. in 2012 UAV photometry is used to monitor a landslide near Grenoble in Southern France. Both orthomosaics and DTMs are created in two instances one and half year apart. By comparing the resulting products a greater insight into the internal dynamics of the landslide is given and flow rates are mapped. In addition comparison to laser scanning yielded similar results. It is also suggested by Niethamer et al. (2012) that soil moisture differences show up in different colorations of the bare soil; this offer perspectives for soil moisture research.

Harwin & Lucieer (2012) used UAV photometry to monitor the erosion of a protected stretch of natural coast in Southern Tasmania. The morphological changes are very subtle and not easily identified on satellite images, so the higher resolution of the UAV photography is necessary. These geomorphologic changes are thought to be a proxy for climate change.

Turner et al. (2012) used UAV photometry to create orthomosaics of arctic moss beds on Antarctica, the spread of which can be used as a proxy for climate change additional images taken at periodically should yield a time series which could expose trends.

Hugenholtz et al. (2013) used UAV photometry to monitor the dynamics of barchan dunes in Southeastern Canada. Ultimately a time series of orthomosaics and DTMs should yield a better understanding of their development and stabilization due to vegetation cover. The quantitative outcomes can be used for parameterization and testing of models representing the dynamic morphology of dunes.

In addition a wide variety of archeological studies have been done. Orthodems can be used to take accurate measurements of the outlines of old ruins and DEMs are used to represent the relief in an area of archeological importance, which can highlight unexcavated structures (Anzhar & Ahmad, 2014).

## 3 Methods

First the gathering of the series of UAV images and DGPS data will be explained. Then, the methodology of processing will be described. And finally the use of a vegetation filter and calculating the gully volumes will be elaborated upon.

### 3.1 Gathering data

This section will explain the field campaign, starting with the selection of the most suitable gullies. Then, the material which was used to acquire the data will be explained. And finally the flight campaign will be discussed.

#### 3.1.1

The following criteria were used for proper gully selection. First and for most **geomorphology**. The scene needs to contain a gully which is certainly part of the third geomorphologic stage as described by Bonnet et al. (2001), meaning it should incise the second stage. The geomorphology of the second geomorphologic stage (see chapter 2.1 Study area) needs to be well preserved, so it is possible to recreate it in GIS for volume calculations. Extra care was taken to interpret the geomorphology of a prospective gully to determine if it is a relic of an older geomorphologic stage or geologic processes. **Accessibility** is important: the distance and the condition of nearby roads, the amount of vegetation in and around the gullies, the steepness of the gully walls and the leniency of possible landowners are all contributing factors. A small open space is needed, which can act as a **base and landing zone** for the UAV and the pilot (Eisenbeiss, 2009). Vision for the pilot is also an important factor; standing at the bottom of the gully for instance it is harder to estimate the scene of the pictures which are taken then when standing at the top. The **Cell phone reception** required for RTK GPS measurements should be available, also in the gully bottom.

Initial selection of gullies was done from Google Maps. Several gullies with 'high potential' were selected for further field investigation. And their map coordinates were relayed to the DGPS service for accurate calculations of differential data.

In the days preceding the flight campaign the selected gullies were investigated in the field because satellite imagery does not contain all the information needed to make an accurate assessment for the proper gully selection. Four out of six gullies which had been picked from Google Maps turned out to be unsuitable. They were either inaccessible, too big or they did not uphold the correct geomorphological criteria. Especially the scale of the gullies was a problem, some of the selected gullies were simply too large to measure and, based on field interpretation, they might have been the cause of geologic faulting as opposed to fluvial incision. Further field inspection of the area revealed two other gully systems which were deemed to be better suited.

### 3.1.2 Materials

#### *UAVs*

For this project two types of UAV platforms were used. The raptor chassis consists of a hard polymer alloy, and it has a wing span of about 2 meters. The EasyStar has a polystyrene chassis and is considerably smaller with a wingspan of 1.37m. The planes are propeller driven, with their electrical engines on the top of the plane in the center, at the location where the wings meet. A cavity in the hull holds the electronics: the battery, the sensor, the autopilot/stabilizing and navigation chips and the receiver. A hole in the bottom of the front of the chassis allows the sensor to capture the scene below. Figure 19 shows the Raptor drone among other field work equipment, on the bottom of the platform a small hole is visible behind which the sensor is located.

#### *The sensor*

For acquisition of the aerial photographs a Canon powershot D10 camera was utilized, see Figure 8. This is a high quality consumer grade 12 megapixel camera, it has a 35mm basic focal length (not zoomed in). This camera was decided upon because of its robustness. It was developed especially to withstand shocks and impacts, and it is able to operate under shaky conditions. Its ability to take photos with a very short exposure time is key to prevent motion blur resulting from the UAVs movements. Image stabilization mechanisms prevent blur due to camera shake which results from engine and atmospheric movements. The sensor is connected by micro-usb to the piloting chip, this allows pictures to be taken both manually and automatically.

Its images are captured in JPEG format which uses a lossy compression which might cause some of the image data to be lost as opposed to PNG and TIFF which are true color image formats, however the file sizes are much smaller, which allows for more easy handling and processing of images.



Figure 8 A Canon D10 camera, used aboard the UAV.



Figure 9, Fieldwork equipment; The RTK GPS, The raptor drone, the black dot on the front of the bottom side of the drone is a whole which behind which the lens of the camera is situated. One of the GCP markers can be seen underneath the black box.

### *RTK GPS*

The DGPS is used to collect ground control points for geocoding images and a second set for accuracy evaluation. The GPS equipment consisted of a pole of exactly 2 meters; on the top of the pole there is a receiver. Mounted on the pole are a: satellite receiver, remote control, bubble level and a modem which connects to the base station. A photo of the RTK GPS is displayed in Figure 9. The remote control is used to insert project parameters, give measurement commands and store the data. The type of antenna used is a R8 GNSS/SPS88x from Trimble.

The items stored for every measurement are: latitude, longitude, northing, easting, height, elevation, vertical precision, horizontal precision, RMS, the name and feature code, and several parameters used for the positioning calculation. Northing and easting and elevation indicate the location in the projected coordinate system, in this case RFG/Lambert 93. Latitude, longitude and height indicate its location in the geographical coordinate system, in this case WGS 84.

Horizontal inaccuracy results from movements during measurement and created by not holding the stick exactly perpendicular to the earth surface. Small variations and movements are exacerbated at the receiver because it is further from the place where the stick touches the ground which is the center of rotation. The text box on the next page explains the inner workings of RTK GPS in detail.

### How does differential RTK GPS work?

Real time kinetic (RTK) GPS utilizes the carrier phase (wave length) of the GPS signal as opposed to the pseudo random noise which is the actual message. Given that the wave length of the signal is known and the phase will change as the satellite moves. The distance to the satellite can be accurately calculated by tracking the phase of the signal over a short time. The amount of wavelengths which have passed between the receiver and the satellite can be approximated using a complex function called the ambiguity algorithm (Bertiger et al., 2010). Using RTK GPS will also negate the effect of selected availability which is part of the pseudo random noise; this is an error inserted on purpose by the United States government to disallow foreign powers accurate missile tracking.

The next part which is needed to create an accurate measurement is the differential data. The satellite's signal will change due refraction anomalies related to atmospheric differences. Differential data corrects for these differences by accurately calculating atmospheric parameters in real time at certain base stations. The DGPS method used for this project is VRS (virtual base station); instead of using the data from one base station, the differential data is interpolated from a model which is created from a grid of nearby base stations.

In addition the signal needs to be corrected using ephemeris, algorithms which account for the changes in the satellites orbit due to the gravitation of sun and the moon.

### *GCP Markers*

Ground control points were cut from rolls of vinyl flooring with an of white bottom which is used as the face up side in the field, in the center a dot is painted using a template and black spray paint. Sadly, overillumination of the markers made the black dots not visible in some of the photographs. In those cases the precise location of the DGPS measurements had to be guessed at the center of the white GCP surface, see Figure 10 for a comparison of two aerial images, one where the dot is visible, and one where it is invisible.



Figure 10 the same marker is shown in two different images recorded in the same flight

### 3.1.3 The flight campaign

The methodology of a flight campaign over a gully is represented schematically in Figure 12. At the gully location, first, the markers were placed at locations in and around the gullies. Markers should be placed on open ground where they can be identified easily in the aerial photographs, and they were distributed evenly throughout the scene. They were fastened in to the ground with stones and nails, so there would be no movement due to wind during the acquisition of the images. The locations of the markers were measured with the RTK GPS either before or after the flights, on the center of the dot on the marker. In addition, referenced points were taken with the RTK GPS in many locations in the field; different feature codes were chosen for different types of geomorphology: slopes, gully bottoms, and plains. This was done so the statistics of the accuracies of the resulting DEMs could be calculated separately for different geomorphology types.

Several modes of image acquisition were available: the UAV could take pictures at a set distance traveled, at a set time interval or at set GPS locations or they could be taken manually using a button on the remote control. The field campaign was hampered by strong wind conditions, see Figure 11, which meant that manual controlled flights were the only viable option. In addition, It

The photos were stored on the flash disc of the camera and uploaded in the field to a laptop. By building a basic model (see chapter 3.2) in Agisoft Photoscan it was possible to assess whether the desired areas were covered and which areas might need to be revisited. A car battery provided the power to charge the UAV batteries and the laptops.

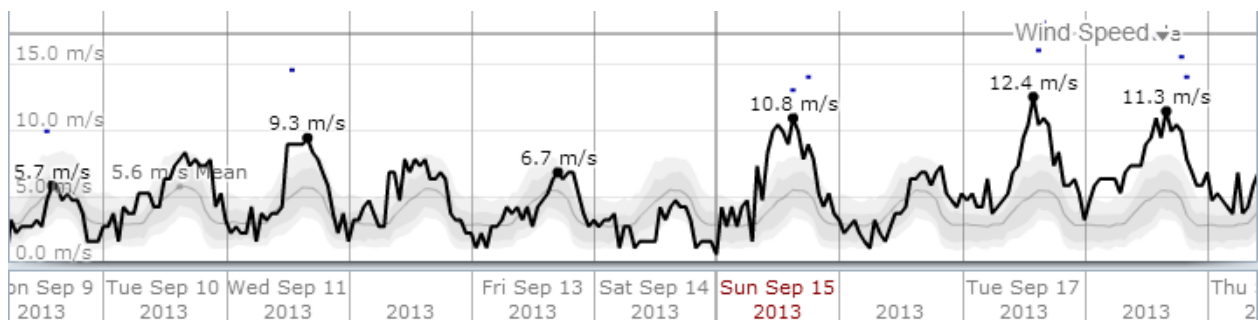


Figure 11, Wind speeds during fieldwork. The estimated wind speed during the flight campaigns often greatly exceeded the 90% percentile for the area. Source: [www. weatherspark.com](http://www.weatherspark.com).

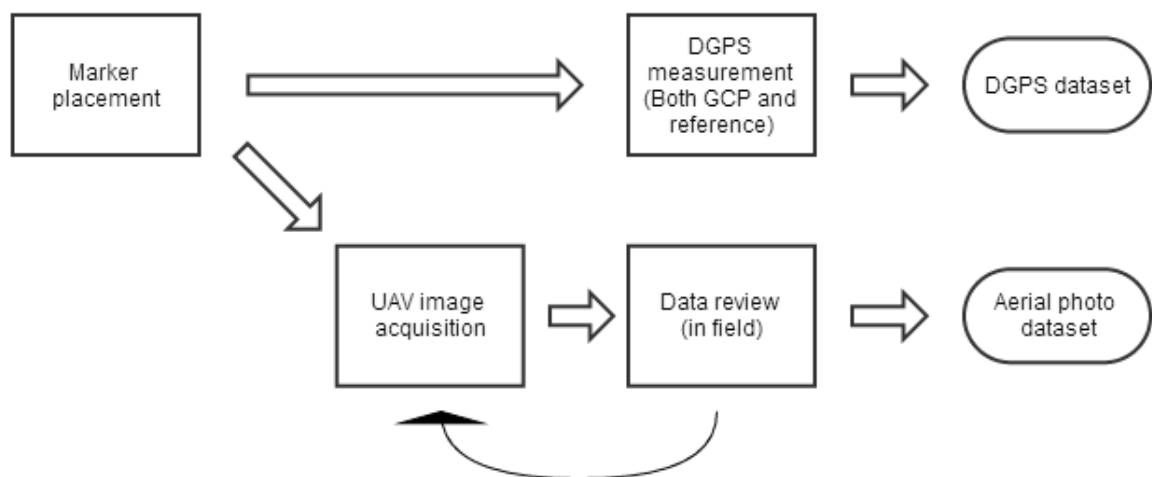


Figure 12 A flow chart of the basic field methodology used to acquire data for the creation of a DEM and orthophoto of a pre-selected gully.

### 3.2 DEM generation

The UAV acquired images were selected on the basis of their quality and overlap. Next, orthomosaics and DEMs were created. Then its accuracy was calculated to determine if the DEM was of desirable quality. Subsequently, the vegetation was filtered, and finally the volume of the gullies could be calculated. This chapter will describe the methodology which was used to create the base DEMs before vegetation was filtered. Processing at this stage was often hampered by the computational limitations, since calculations done in Agisoft require large amounts of processing power, time and disk space.

DEM generation is the first and most extensive phase of the process. A flowchart of the DEM generation process can be found in Figure 13. For this phase Agisoft Photoscan was used, a proprietary software, which allows for the creation of 3D models and orthophotos from 2D imagery; and it is well suited for the processing of UAV areal images and ground control points. Agisoft allows for DEM creation by joining separate DEMs called chunks. Each flight dataset made up a separate chunk. All gully DEMs are made from 2 or three of these chunks corresponding to different flights.

In the first phase the poor quality photographs are excluded. Blurry photos, photos which were taken at an elevation which is too low and photos which clearly contain the wrong scene are removed. Next, the qualified photos are loaded into Agisoft, and an initial model is built with a low resolution to give an overview of areas which need to be cropped or masked. The following steps are made create a basic model in Agisoft Photoscan, some of the terms used here are further explained in chapter 2.4:

1. Photo alignment; a mosaic of the overlapping images is created using feature matching of overlapping image pairs. The mosaic represents on big picture of the scene. In addition a basic bundle block adjustment is done to create the locations of the points in the point clouds in a low quality 3D spatial environment.
2. Build dense cloud; this preforms a more intensive bundle block adjustment which can be done at several quality scales. Although the highest intensity setting would cause the computer's RAM to become overloaded. The result is a more accurate point cloud with much more points.
3. Build mesh; this builds a TIN model from the initial cloud or the dense cloud. The amount of faces chosen specifies the amount of triangles in the TIN which are used to recreate the scene.

Next, the photos are reassessed and large vegetated areas, water, people and areas outside of the wanted scene are masked. Masking out large vegetated areas will ensure that the faces, the triangles which make up a vector DEM (TIN), will not be used for building vegetation geometry, which is complicated and will be filtered out anyway. During the masking process some more undesirable photos might be omitted.

Then, the model is rebuilt on a higher resolution and this time the texture is also computed. This allows for the white markers which indicate the ground control points to be identified. Marker points are then placed inside the model. The program automatically filters the photos per marker and places markers in the photos at the estimated locations. The markers are then dragged manually in to their correct places in the photographs one by one, a tedious task which was hampered by image quality as is shown in Figure 10.

Then, the GCP coordinates are imported and linked to the correct points in the images. To import the GCPs the DGPS data first had to be modified and prepared in the proper Comma delimited values (CSV) format, see appendix J. The names of the DGPS points were changed to the names of the corresponding points in the Photoscan project. A Helmert transformation was then applied to fit the model to its new coordinate system and to make the model more accurate: using the locations of the GCPs as the ground truth. The model was then recomputed with the optimal settings. Chapter 5.1 shows how these optimal settings were determined. The software automatically computes the accuracies of the GCPs with respect to each other and their estimated points in the different photographs. This allowed for fast error checking; GCPs which showed unnaturally large error were deleted.

Finally the different DEM chunks were joined by joining the overlapping GCPs. To complete the model, the last phase of the model building process, the mesh creation, was redone at optimal settings.

The DEMs were exported to a TIFF raster format at the default resolutions, between 1 and 5 centimeters depending on the DEM. Resolutions for the orthophotos tend to be half those of the DEM by default. It is possible to export it as a TIN format also, however this provided difficulties at the vegetation removal and gully volume calculation stages.



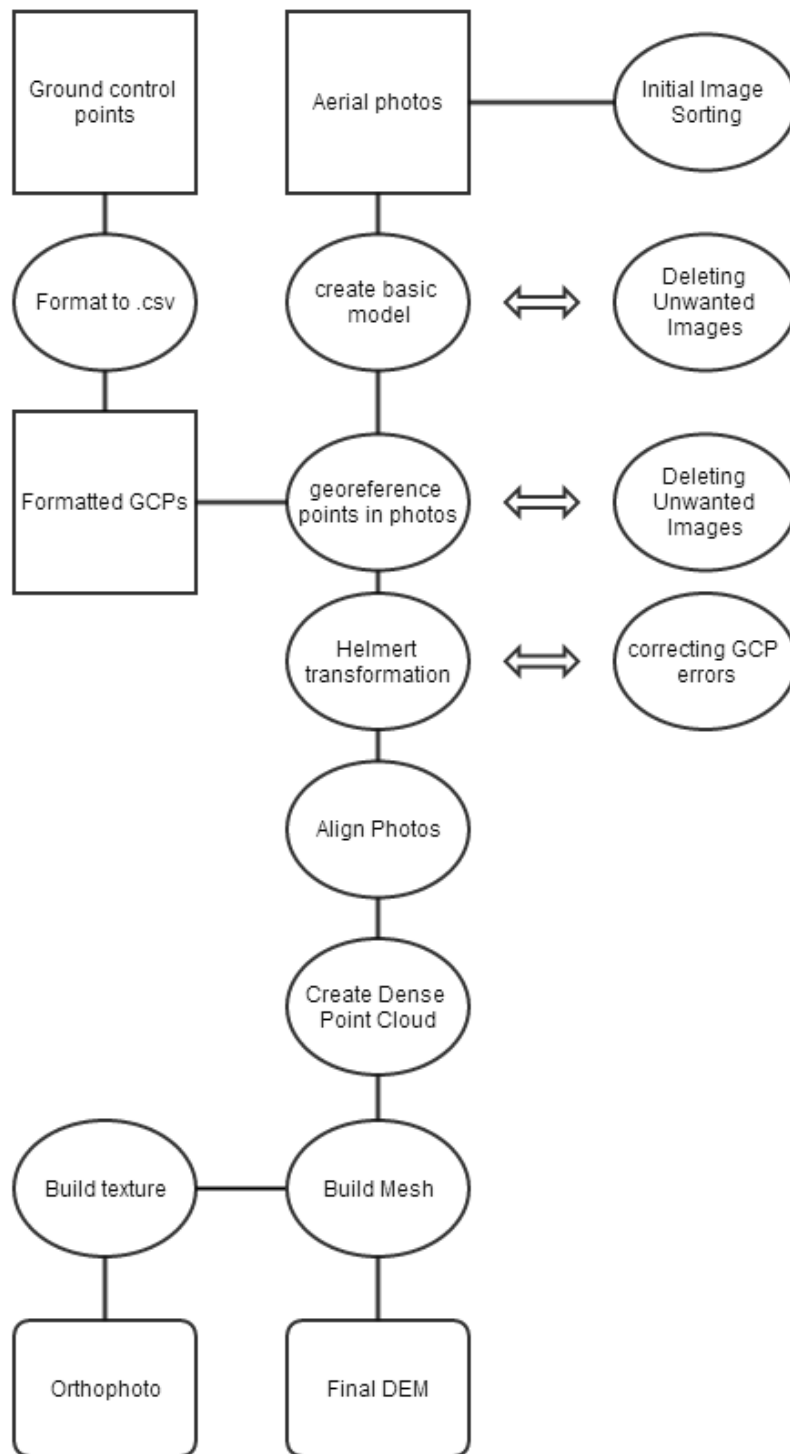


Figure 13 A flow chart of the DEM generation process. It starts at the top with the raw data which is processed to a DEM and Orthophoto. The removal of images recurs several times in the process to obtain the best dataset.

### 3.2.2 Accuracy analysis

Accuracy analysis occurred at several stages of the project. The accuracies of DEMs created with different interpolation settings were explored, to obtain the best settings. And, accuracy analysis was performed on the final DEMs. During acquisition of the reference point data a distinction was made between several parts of the gullies. this allows their accuracy to be calculated separately, and gives information on the differences of accuracy within a single DEM.

#### *Calculating the accuracy of a DEM*

Due to the fact that the center dots of the markers were not clearly represented in many of the photographs, it was not possible to do a lateral accuracy analysis on the orthophotos. So, the accuracies calculated are only vertical accuracies. Figure 14 shows a flowchart of the accuracy calculation process.

The first step was creating a character separated value file of the test point data which could be imported into a GIS environment, see [appendix x](#) for an explanation on creating CSV files. Next, both the test points and the final DEMs were imported in GIS and the DEM height values were extracted at the reference point locations. Both values were subsequently exported and processed further in Python. A script calculated various statistics based on the height differences between reference points and the DEMs, see Appendix A for the script. In addition, because the reference points were fitted with feature codes which correspond to different geomorphological features it was possible to calculate these statistics separately for groups of test points within one DEM. The script calculates the average, median, standard deviation, RMS, minimum and maximum the entire DEM and for the different feature codes.

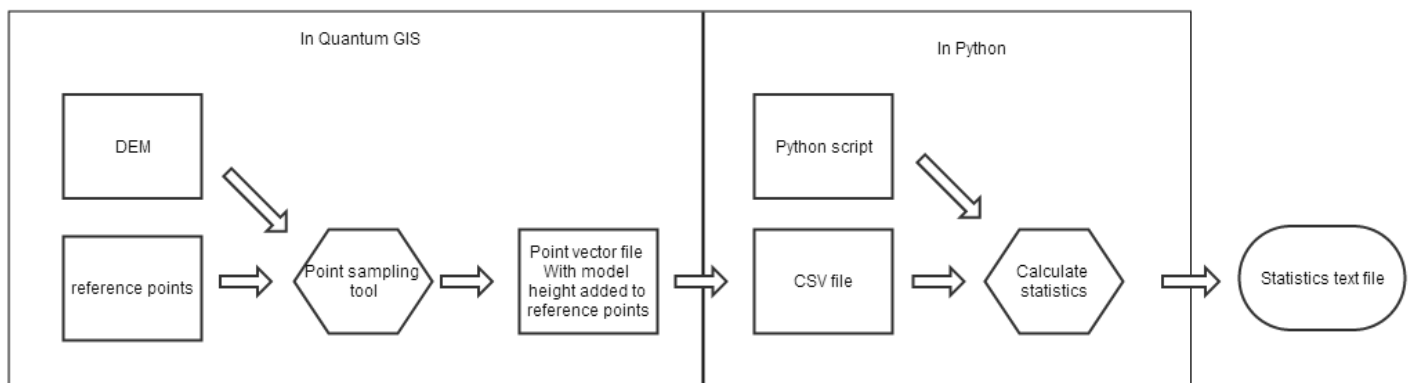


Figure 14, flowchart calculating vertical accuracies

#### *Obtaining optimal settings*

In order to acquire the optimal settings for DEM generation a series of test runs were made using different settings and their results were evaluated. To reduce processing times the smallest gully data set was chosen for this. Agisoft Photoscan features the possibility to “batch process” its functions using a python script.

### 3.3 Calculating gully volumes

The basic idea behind calculating the volume of gully is: Creating another DEM which is fitted over the gully and subtracting the gully DEM from it. The difference yields the gully volume. For accurate gully volume calculations the vegetation should be removed from the DEMs first, thereby creating digital terrain models (DTM), which represent the ground surface only.

No viable vegetation filtering methods were found in literature so a custom vegetation filter was developed for the purpose of this project. The filter works by interpolating new height values from the sides of the unwanted vegetation area. The same filter was also used to create the DEM which were fitted on top of the gully for the volume calculations. Therefore the vegetation filter will be described extensively first. The final filter was the results of a long search in which many methodologies were tested but deemed unviable.

#### 3.3.1 The vegetation filter

Vegetation filtering consists of two phases: identifying vegetation and removing vegetation. The objective of vegetation identification is creating a vector file with polygons overlaying the vegetation patches, which can be used for the final filter. Vegetation shows up as bumps on the hillshade model and it is easily identified visually in the orthophoto. Manual identification of vegetation was done by drawing polygons over the vegetation patches by hand, using both orthophoto's and a hillshade model as basemaps. Figure 17 shows the Vailhes gully with polygons on top of the vegetation which is to be removed.

##### *Vegetation removal*

This part describes the vegetation filter which was used to produce DEMs with the vegetation removed, which are fit for accurate gully volume calculations. In addition, an adaptation of the same method was used in the volume calculation. This method was designed specifically for this project. The filter has been created by connecting a chain of operations in the ArcGIS model builder. An overview of the process is given in Figure 16.

The input consists of the vegetation polygons acquired from the vegetation identification process and the original DEM with vegetation. First, A buffer operation was done on the vegetation polygons, this yielded a vector file with rings of one meter surrounding the vegetation. Next, inside these rings a large number of randomly generated points were placed. Then, the values of the DEM were extracted at these locations. Subsequently, a new DEM interpolation was done which used the extracted values as input and the original DEM as extend and resolution. The interpolation method which was deemed most suitable was the natural neighbor, although it does leave a checker boarded pattern visible on the hillshade model, as the result of the process; the results of other interpolation methods such as: Spline, trend and IDW were much poorer. In the new DEM only the vegetated spots are smoothed as if the vegetation was not there, the region outside of these spots holds no value. To include these new spots filtered of vegetation in the original DEM, the spots were extracted using the extract by mask option on the new DEM, wherein the vegetation polygons are used as the mask. This process yielded a raster with only the smoothed over vegetated spots and NoData values for the other cells. Finally, by using the Mosaic function the vegetated spots were overwritten with the filtered spots while the rest of the original DEM remained intact. Figure 15 indicates the result of this vegetation removal method for a shrub on a sloped area. Figure 17 is a collage of six images focusing on the same part of the DEM and orthophoto. It shows the how the polygons are overlaid on the

vegetation and how the DEM looks before and after, and it shows how hillshade models of before and after the interpolation, revealing the checkerboard pattern. However on the actual DEMs it appears smooth.

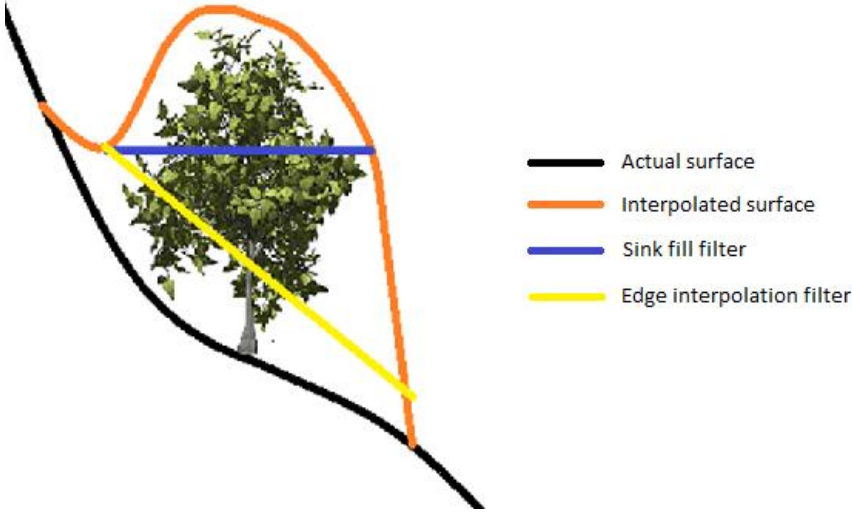


Figure 15 Results of the edge interpolation filter. It represents the way the faulty(orange) interpolated surface is cut off by the vegetation filter (yellow). The sink fill method (blue) was one of the unsuitable alternatives explored. It relied on reversing the DEM and filling the sinks, hence the straight cutoff.

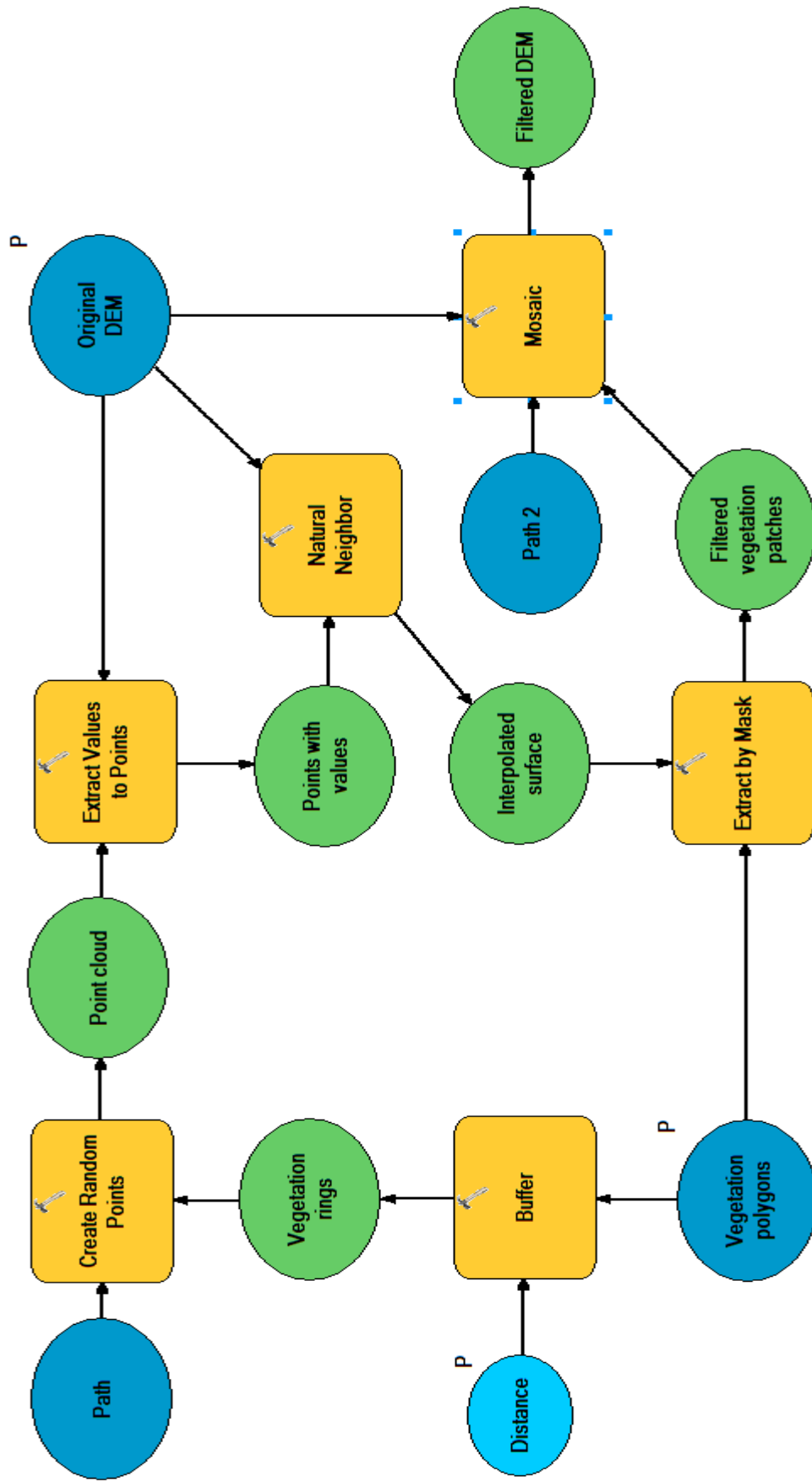


Figure 16 A flow chart of the vegetation removal using interpolation from the edges of the vegetated patches

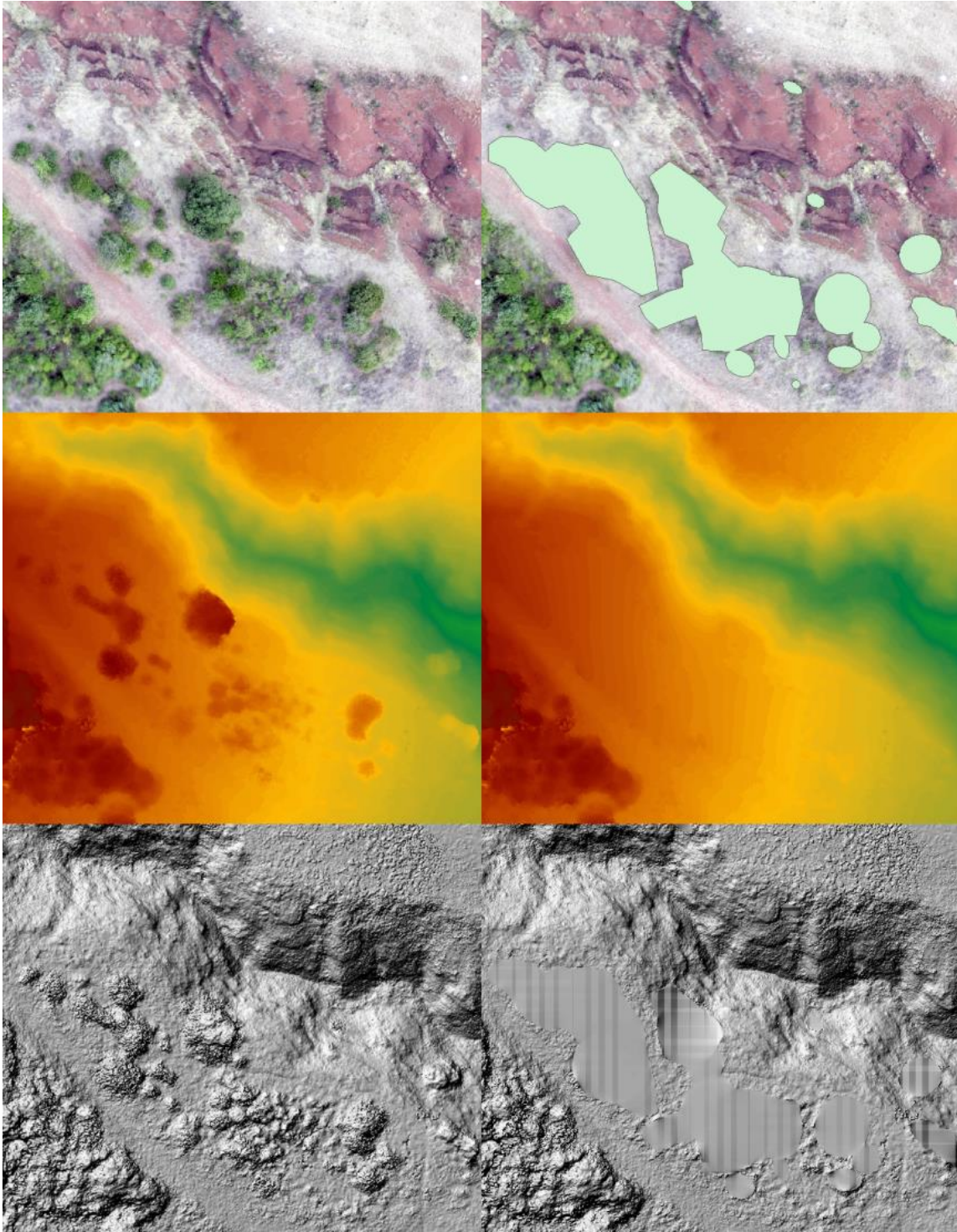


Figure 17, A collage of image showcasing the vegetation filter.

Top-left: the orthophoto. Top-right: the orthophoto with vegetation covering polygons. Center-left: original DEM. Center-right: DEM filtered using edge based removal. Bottom- left: hillshade model of the original DEM. Bottom-right: hillshade model created after edge interpolation. The checker board pattern is an artifact of the DEM interpolation method which was used and the subsequent mosaic operation.

### 3.3.3 volume calculation

This part describes the approach to calculate the gully volumes, the final goal of this thesis. The method consists of two phases. First, the geomorphology of the landscape before incision (second geomorphologic stage) has to be constructed. And finally, the original DEM needs to be subtracted from the second stage to calculate the volume.

#### *Reconstructing paleogeomorphology*

The reconstruction of the topography as it was before incision can be visualized as a lit over the gully, a curved plane which joins the edges of the gully in an optimal way. A flat or linear inclined plane would be easy to create. However, although it would approach a solution, it does not suffice for the objective of this thesis since the second geomorphologic state was not linear. To reconstruct the second stage the edge interpolation method which was used to remove the vegetation was adapted to create the plane over the gully.

Instead of inserting polygon cover mask of the vegetated spots, a vector cover map for the gully was created and used as input. The gully cover polygon was made manually; the edge of the polygon corresponds to the edge of the gully. The gully edges were estimated from the Orthophoto and the hillshade model of the original DEM. Small errors at the top of the gully can lead to large errors in volume. Due to its change in width most of the volume of a gully is located at the top of the gully, so errors in drawing the gully cover polygon might significantly skew the volume calculation.

#### *Calculating volume*

The final step in the process, uses the vegetation filtered DTM and the reconstructed second stage as input. The volume can be calculated by subtracting the two elevation models and determining the volumetric difference. For this two methods have been identified, both utilize ArcGis.

The cutfill method yields a 2 dimensional raster wherein the volumes are calculated by area, both negative and positive. This method can also be used to verify the accuracy of the gully cover. Negative volumes appear on the side of the gully in some cases if the cover is drawn too wide. The landscape on the side of the gully does not form a perfect plane so it will be higher than the gully cover DEM in some places, this shows up in the cutfill as negative volume. One condition for the cutfill method is that both rasters have to have the same cell size and extend.

“EnterVol” is a proprietary ArcGis plugin which enhances the 3D capabilities. It has a volume calculation method wherein the different DEMs do not need to have the same cell size and extend. In addition it provides a mesh, which is great for visualization. This method allows you to define the resolution of the mesh yourself, however high resolutions cause it to fail. Because the cutfill method was provided and end result of much higher resolution and thus accuracy it was used for the final volume estimates. “Entervol” does however provide great meshes for visualization purposes. Figure 9 shows a collage of images explaining the volume calculation process.

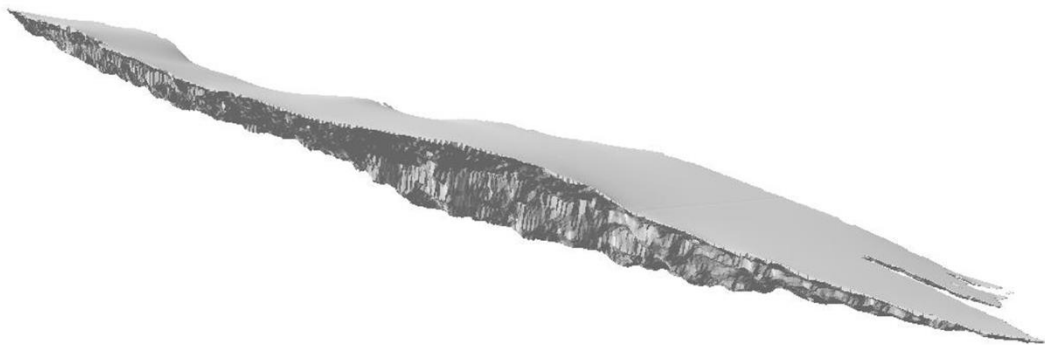
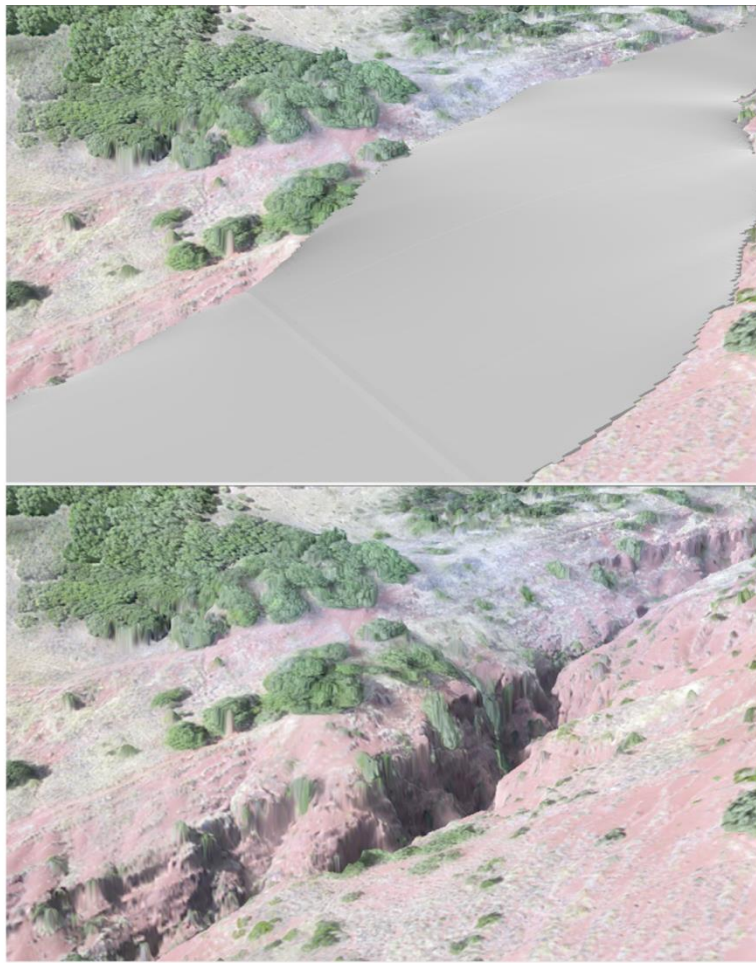


Figure 18 a collage of images explaining the volume calculations. Top: the orthophoto overlaid on the DEM with the vegetation removed. Middle: the same orthophoto as the top image with the an interpolated surface on top of the gully. Bottom: a mesh which shows the gully volume made using Entervol tools.



## 4 Results & Discussion

Four gullies have been selected based on the criteria of geomorphology and accessibility. In this chapter gullies will be described and the results of the DEM construction of these four gullies. In addition, the accuracies and the volumes will be given and discussed.

Table 6 provides an overview of the geomorphologic characteristics of the four gullies. Table 7 displays the area, volumes and average depth of the gullies, and a comparison to the volume of Olympic swimming pools to make the numbers more tangible. The data in the tables will be discussed separately in their respective gully subchapters. In these the gully geomorphology, DEM construction, accuracy analysis and volumes will be elaborated upon separately. Appendix X provides an overview of all the tables in this chapter which can be used for comparing the gully data. The orthophotos of the gullies can be found in the appendices as well.

In chapter 4.2 the resulting accuracies of the gullies will be compared to each other and to accuracies of photogrammetric DEMs constructed for other studies. In addition several aspects of the methodology and their alternatives will be discussed.

**Table 6, overview of gully geomorphology. The numbers are estimated averages based on measurements in GIS.**

Gully	Length	Max. Depth	Width	relief	Vegetation cover	slopes
<b>Brenas</b>	450	25	100	100	Medium	Steep
<b>Celles</b>	320	8.5	30	50	Low	Mild
<b>Salagou</b>	250	30	70	70	High	Very steep
<b>Vailhes</b>	170	8.5	25	30	Low	Mild

**Table 7, results of the gully volume calculations. Based on GIS calculations. An Olympic swimming pool has a volume of 2500 cubic meters.**

Gully	Area	Volume(m <sup>3</sup> )	Olympic swimming pools	Average depth
<b>Brenas</b>	20105.05	109486.81	43.8	5.45
<b>Celles</b>	14386.16	40190.13	16.1	2.79
<b>Salagou</b>	14370.48	79730.89	31.9	5.55
<b>Vailhes</b>	5074.66	11735.81	4.6	2.31



Figure 19, picture of the Vailhes gully

#### 4.1.1 Vailhes

The Vailhes gully was the smallest of the measured gullies, it drains towards the east into the Salagou lake, it is located next to the hamlet of Vailhes. The descent is about 30 meters over an length of 170 meters. It has an average width of about 20 meters. The bottom of the gully exhibits slight meandering pattern. In addition it features only little vegetation, mostly shrubs and a couple of trees at the outflow point next to the lake. And it has very easy accessibility as its slopes were steep enough to walk up or down in most places. Around this gully the second geomorphological state is very well visible, it occurs as a linear plane with a very small inclination towards the southeast. Figure 30 shows this relatively small gully with little vegetation, the same can be seen on the orthophoto in appendix D.

The DEM for this gully was created from two separate chunks focusing on the upper and lower parts of the gully. In all 94 aerial photographs were used and 23 GCPs, see table 8. Three different geomorphological features were distinguished in the field for test point sampling: the gully bottom, the flanks and the slopes. Figure 31 shows the DEM of this gully with the errors at the test point locations. The large positive errors are exclusively found in the gully bottom and at the outflow point where some large trees are located. The boxplot also reveals these large positive outliers. The largest errors appear at in the bottom of the gullies. Table 9 shows much higher medians and RMS at gully bottoms as well. Although the slopes are on par in accuracy with the flanks of the gully they do exhibit a slightly larger variation.

The volume of this gully has been calculated at 11735.81 cubic meters, 4.6 Olympic swimming pools. And, the area of the gully is 5074.66 square meters.

Table 8, Data used for constructing the Vailhes gully DEM

	Chunks	Aligned photos	GCPs
<b>Vailhes</b>	<b>Combined</b>	<b>94</b>	<b>23</b>
	Lower	51	10
	upper	43	19

Table 9, Accuracy of the Vailhes gully DEM

	geomorphology	reference points	Average	median	STD	RMS	min	Max
<b>Vailhes</b>		<b>60</b>	<b>0.078</b>	<b>0.026</b>	<b>0.196</b>	<b>0.211</b>	<b>-0.22</b>	<b>0.82</b>
	gully bottom	20	0.23	0.159	0.252	0.341	-0.085	0.819
	flanks	25	0.011	0.007	0.085	0.086	-0.219	0.144
	slopes	15	-0.011	-0.038	0.107	0.107	-0.148	0.221

Vailhes: DEM and error

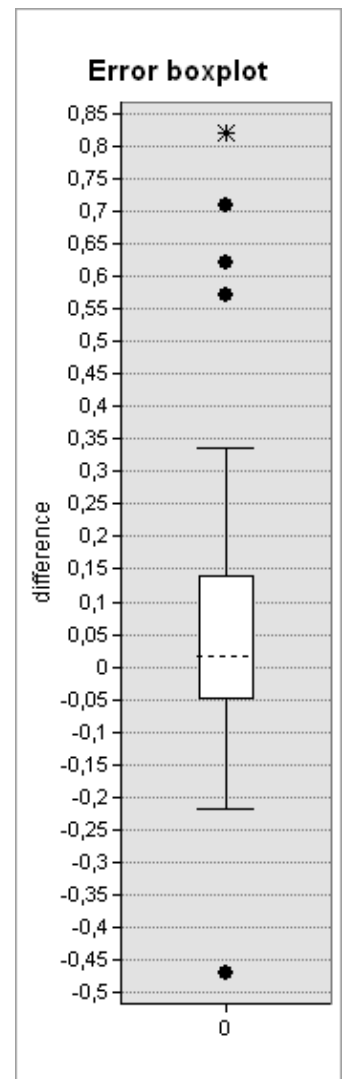
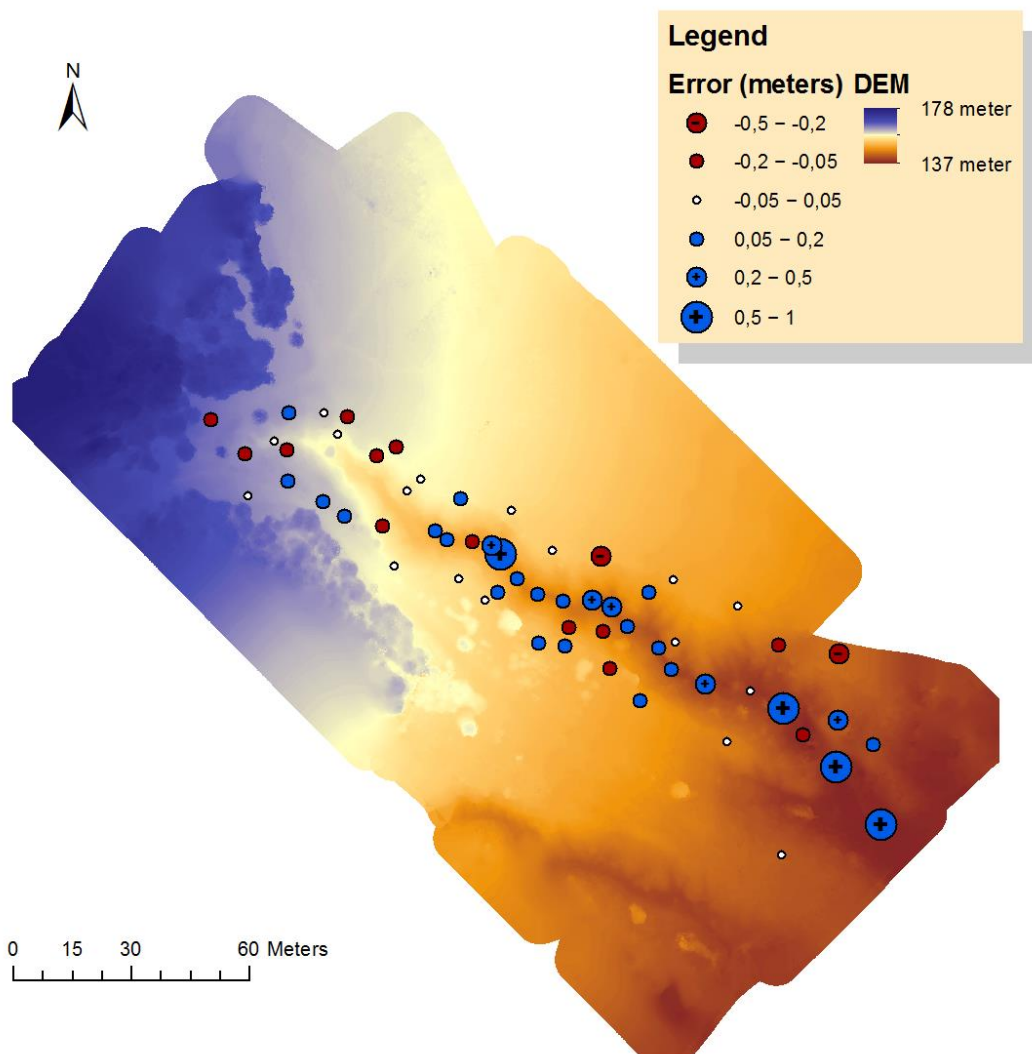


Figure 31, The DEM

of the Vailhes gully. The boxplot uses the points visible on the DEM as input data.

### 4.1.2 Celles

The geomorphology of the Celles gully is similar to that of the Vailhes gully except with 320 meters it is much longer. This gully drains towards the southwest; its outflow point is on the beach near the Salagou Lake. Its named after the ruined village of Celles which is located next to it. The gully is easy to access; in most part you can just walk in from the sides. The slopes are not very steep. It features some small tributaries and it is forked in the beginning. The beginning is obscured by a row of trees and bushes, however the rest of the gully only features a small amount of vegetation. The orthophoto found in Appendix E shows the gully as it is just described.

From 4 successful flights, the two most complete data sets which complement each other in the best manner were chosen. In total 79 aerial photos were used with 40 markers, see table 10. The test points of this gully are subdivided into three classes based on their geomorphology: the gully bottom, the flanks and the slopes. Figure 32 shows the DEM with the errors at the test points. The DEM contains some edge effects in the northeast, the reference points at this location have been cropped. In addition the DEM has been smoothed over using the vegetation filtering algorithm, in some places on the sides where the large errors occurred. The errors in the north of the DEM are the result of poor aerial imagery coverage, for these locations only a few descent photos were available. Figure 32 shows most positive errors on the slopes and negative errors on the slopes of the DEM, table 11 also reflects this. The accuracy on the slopes is even higher than on the flanks. This could be related to vegetation on the flanks or poorer aerial photo coverage. The boxplot looks a bit like the one from Vailhes, with the median error of 3-4 cm and the tails at between 20 and 30 centimeters plus and minus, both have very high accuracies.

The volume of this gully has been calculated at 40190.13 cubic meters, 16.1 Olympic swimming pools. And, the area of the gully is 14386.16 square meters.

Table 10, Data used for construction the Celles gully DEM

	Chunks	Aligned photos	GCPs
<b>Celles</b>	<b>Combined</b>	<b>79</b>	<b>40</b>
	Lower	36	21
	Upper	43	32

Table 11, Accuracy of the Celles gully DEM

	geomorphology	reference points	Average	median	STD	RMS	min	Max
<b>Celles</b>		<b>96</b>	<b>0.036</b>	<b>0.033</b>	<b>0.16</b>	<b>0.164</b>	<b>-0.5</b>	<b>0.528</b>
	gully bottom	24	0.088	0.059	0.122	0.15	-0.098	0.494
	flanks	42	0.025	0.023	0.155	0.157	-0.5	0.356
	slopes	30	0.009	-0.049	0.182	0.182	-0.275	0.528

Celles: DEM and error

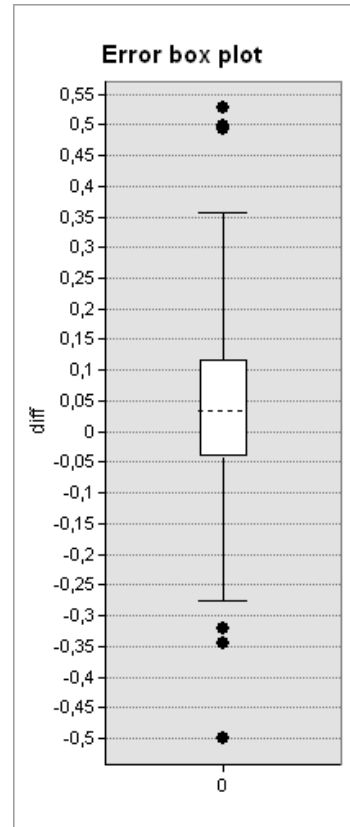
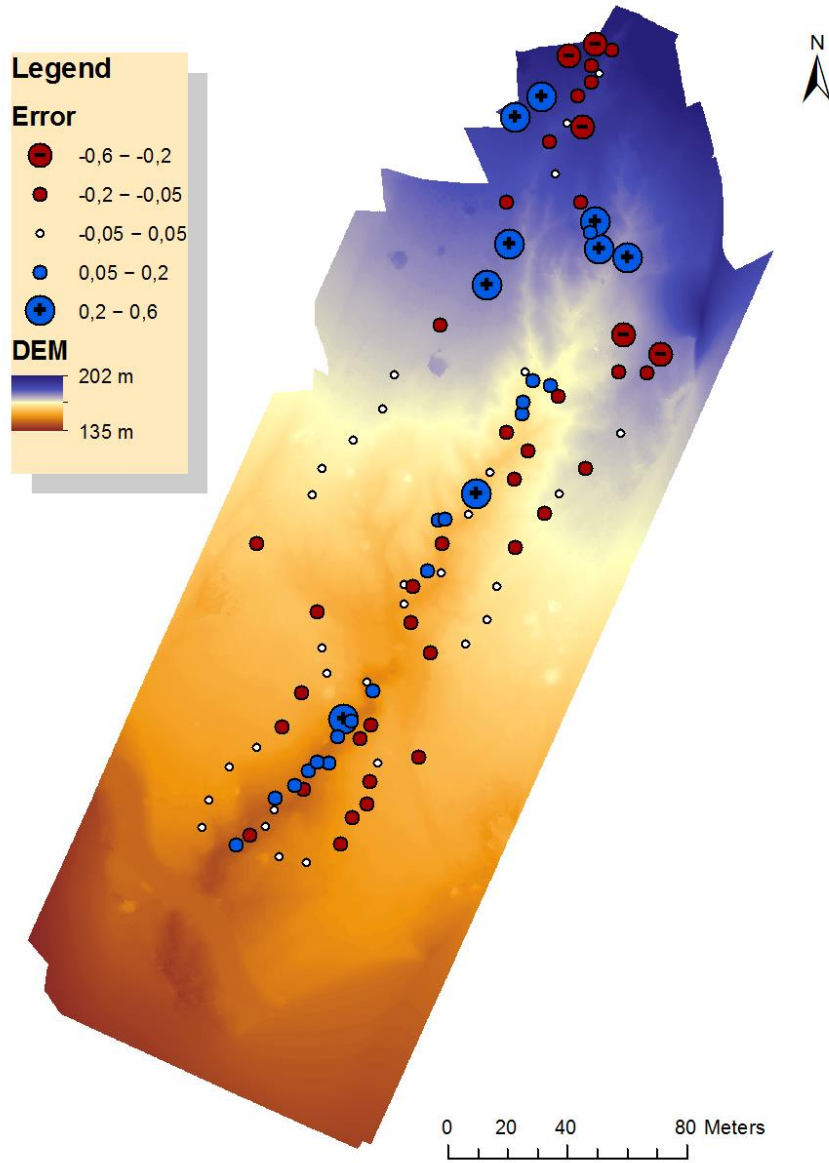


Figure 32, The DEM of the Celles gully. The boxplot uses the points visible on the DEM

as input data.



Figure 33, picture of the salagou gully

#### 4.1.3 Salagou

With a descent of 70 meters vertical over 250 meters length, the Salagou gully is the steepest of the measured gullies. Its relief is its defining characteristic compared to the other gullies. Not just the descent but also the slopes of the gully were very steep; with a maximum depth of over 30 meters this is also the deepest gully. Its width varies as it becomes much wider at the outflow point. It has been named after the Salagou lake in which it drains, and it is located close to the ruined village of Celles. The gully cuts itself into the hillside quite high up, much higher than the Vailhes and Celles gullies, which cut into the same hill. The gully contains a lot of vegetation, mostly trees, especially on the sides; this made estimating the gully edge quite difficult. In addition, the gully bottom contained a lot of vegetation, from small shrubs higher up to larger trees on the beach at the outflow point. The occurrence of the second geomorphologic stage is not as clearly defined at this gullies as with the others; Its steep relief and thick vegetation

cover make it hard to define a plane which corresponds to the relief before incision. The orthophoto (appendix F) provides an aerial overview of the gully which displays its steepness and large amount of vegetation cover.

The DEM for this gully was created from 3 separate chunks focusing on the upper, middle and lower parts of the gully. In all, 153 aerial photographs were used and 20 GCPs, see table 12. Figure 35 shows the DEM with the errors at the reference points. Because the slopes were inaccessible due to their steepness only two classes of reference points were used: the gully bottom and the gully flanks, beyond the edge. Not the entire gully bottom was accessible for reference point measurements so the reference points in the gully were only taken until about half way, after which the terrain became too steep and inaccessible. The same goes for the GCPs inside the gully.

Looking at the east side of the DEM higher up the hill there are a lot of positive errors. In this location there was a lot of grass which could explain the positive errors there. On the opposite side where the errors are lower and somewhat negative the ground was much more barren. The highest errors can be found in the gully bottom, these are quite high positive errors, the highest of which exceed one meter. The boxplot in figure 34 also accentuates these outliers.

The volume of this gully has been calculated at 79730.89 cubic meters, 31.9 Olympic swimming pools. And, the area of the gully is 14370.48 square meters.

Table 12, Data used for constructing the Salagou gully DEM

	Chunks	Aligned photos	GCPs
<b>Salagou</b>	<b>Combined</b>	<b>153</b>	<b>20</b>
	Lower	56	13
	Middle	58	16
	Upper	39	11

Table 13 Accuracy of the Salagou gully DEM

	geomorphology	reference points	Average	median	STD	RMS	min	Max
<b>Salagou</b>		<b>59</b>	<b>0.162</b>	<b>0.096</b>	<b>0.333</b>	<b>0.371</b>	<b>-0.454</b>	<b>1.361</b>
	gully bottom	14	0.448	0.268	0.399	0.599	-0.01	1.361
	flanks	45	0.073	0.037	0.251	0.262	-0.453	0.731

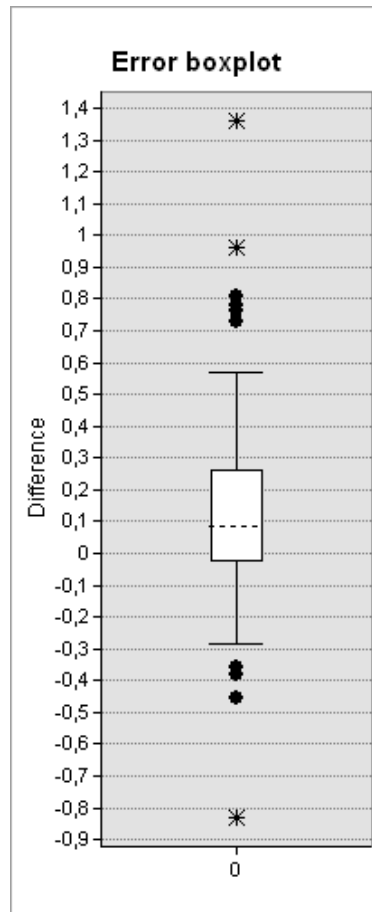


Figure 34, The DEM of the Salagou gully, and the boxplot which was created from the reference points visible in the DEM.

### Salagou: DEM and error

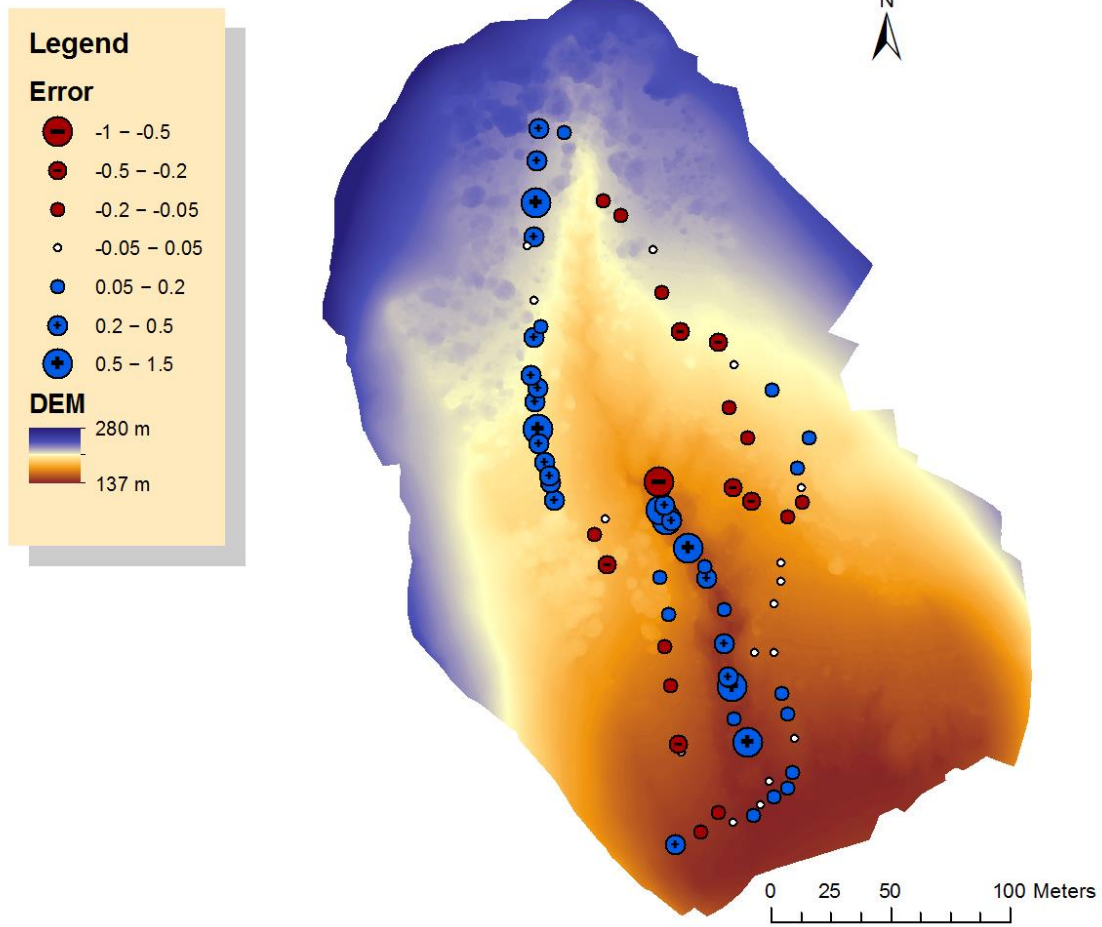


Figure 34, The DEM of the Salagou gully, with reference points.





Figure 35, picture of the Brenas gully.

#### 4.1.4 Brenas

With its 450 meters length this is by far the biggest of the measured gullies. It is also the widest and due to its length it has the highest descent. It is named after the village of Brenas which is located uphill from the gully. This gully is the only gully measured which does not exit directly into the lake; instead, the gully follows a slightly curved path, draining to the south into the Salagou river. Its geomorphology is also somewhat different and more complicated than that of the other gullies. The gully appears to be cut in the lowest point of a pre-existing valley. On the east and north eastern sides there are two prominent peaks which are thought to be remnants of the first geomorphologic stage. The start point of the gully is hard to define; at the top it is flanked by medium steep slopes on all sides which increase in height towards the north east. In addition a small wall has been found which holds back the soil this indicates that the geomorphology has been influenced. A small ridge cuts through the gully here creating a fork; the ridge can be found further down in the valley as well where it continues as the eastern edge of the gully. Small gully like features can be found at the other side of the ridge as well; these are considered to be tributaries to the main gully. An orthophoto shown in appendix G displays the appearance of the Brenas gully.

As a result of its size and due to the bad wind conditions, data acquisition for this gully was especially difficult. The dataset featured many images which had to be omitted due to wind or engine noise or because they were too oblique. Especially the middle and upper parts were hard to acquire. In addition, due to the size of this gully the photos were taken from a much greater altitude. The lower chunk was made from a very big dataset, and it incorporates by far the largest part of the gully. The middle and upper chunk are located quite close to each other at the head of the gully. With only 7 GCPs the ground control coverage of the upper chunk is quite poor. Table 14 gives an overview of the data used to create the chunks and the final elevation model.

Figure 37 shows the DEM with the errors at the test point locations. Because the flanks are quite different in appearance, a division has been made between the western and eastern flanks. A unique geomorphological feature compared to the other gullies are the tops of the small ridge, this has also been measured separately. In all there are 5 classes of test points for this gully including the gully bottom and the slopes. Unlike the other gullies it is estimated that the largest errors in this DEM, which are located almost exclusively in the northeast, are a result of the DEM creation process. Overlap between the upper and middle chunk was very small; and the upper chunk suffered from poor GCP coverage. Table 15 displays another difference in the error distribution compared to the other gullies. The gully bottom does not exhibit significantly higher errors. Errors on the sides were larger due to large vegetation cover and errors in the gully itself are lower because it is relatively flat and wide. The boxplot (Figure 36) exhibits a relatively large distribution in the errors.

The volume of this gully has been calculated at 109486.81 cubic meters, 43.8 Olympic swimming pools. And, the area of the gully is 20105.05 square meters.

Table 14, Data used for constructing the Brenas gully DEM.

	Chunks	Aligned photos	GCPs
<b>Brenas</b>	<b>Combined</b>	<b>236</b>	<b>41</b>
	Lower	127	36
	Middle	40	11
	Upper	69	7

Table 15, Accuracy of the Vailhes gully DEM

	geomorphology	reference points	Average	median	STD	RMS	min	Max
<b>Brenas</b>		<b>159</b>	<b>0.178</b>	<b>0.123</b>	<b>0.237</b>	<b>0.297</b>	<b>-0.208</b>	<b>1.230</b>
	gully bottom	19	0.101	0.132	0.147	0.178	-0.169	0.439
	eastern flank	32	0.223	0.175	0.213	0.308	0.002	0.936
	western flank	56	0.143	0.122	0.185	0.234	-0.208	0.722
	slopes	25	0.172	0.107	0.29	0.337	-0.109	1.23
	central high	27	0.256	0.153	0.315	0.406	-0.05	1.213

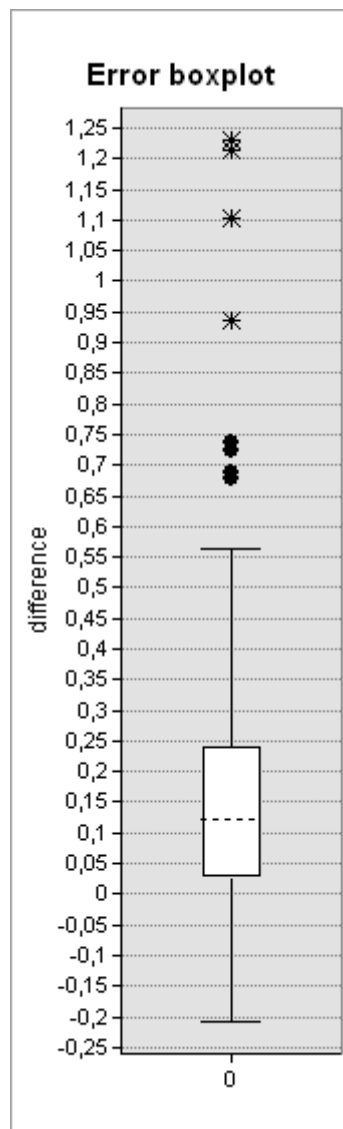


Figure 36, Boxplot of the Brenas gully, errors are mostly positive.

### Brenas: DEM and error

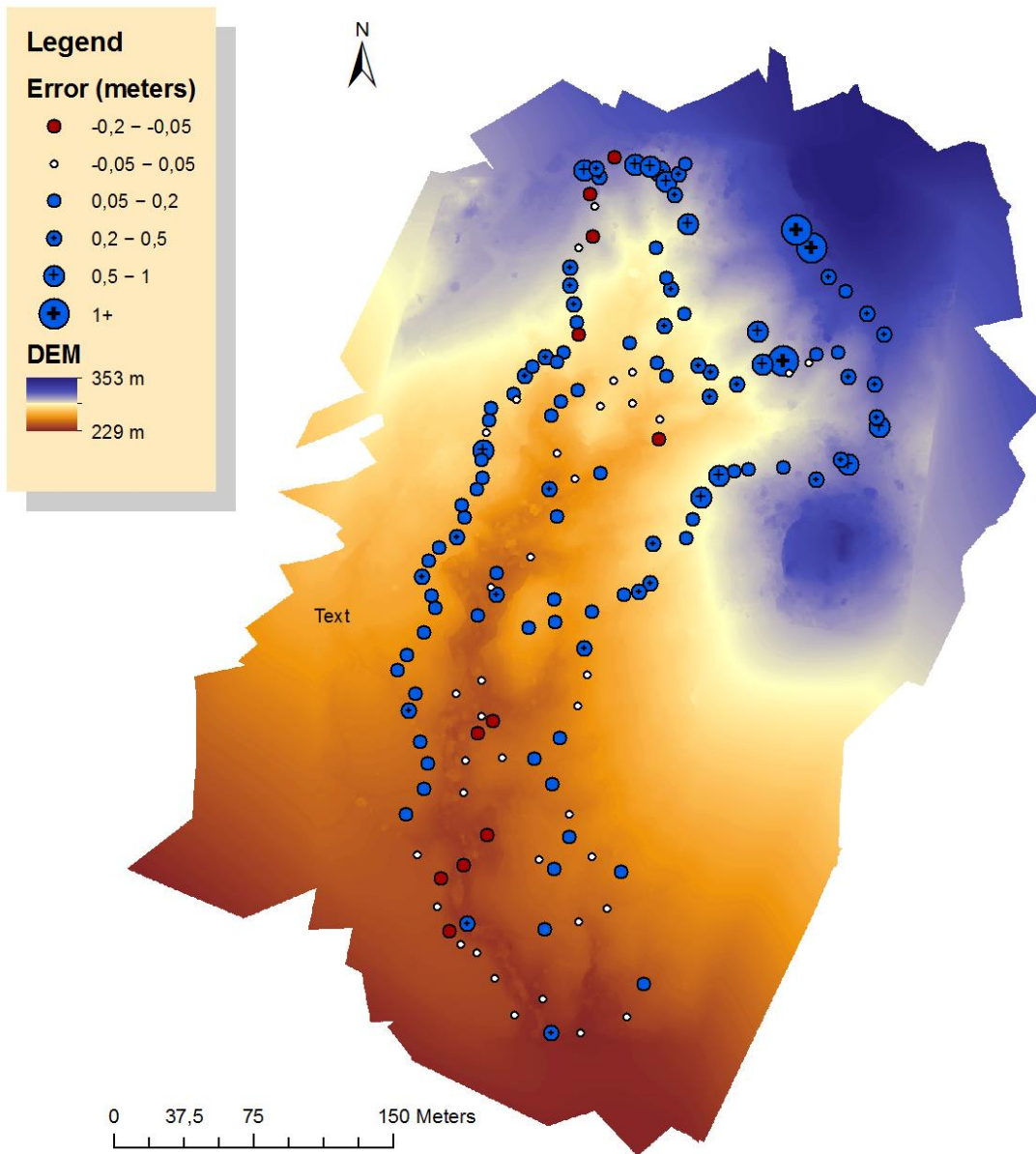


Figure 37, The DEM of the Brenas gully, and the boxplot which was created from the reference points visible in the DEM.

## 4.2 Discussing accuracy

When determining the precision of a DEM, the median is a better indicator of the accuracy than the average because the average is skewed significantly by outliers. In addition, the overall accuracies are of little value if one does not take into account the distribution of the test points by location with respect to their geomorphology. To compare the DEMs it is better to compare the statistics of corresponding geomorphologies. However this approach comes with its own problems because the geomorphologic features are not uniform in the different gullies. For instance the gully bottom of the Salagou bottom is much deeper and its slopes much steeper; this yields a larger error for that class than the gully bottoms of the shallower gullies. In addition the flanks of the Brenas gully featured a lot of shrubs and tall grass increasing the error there; whereas the flanks of the Celles and Vailhes gullies were mostly barren with some low grass.

It seems that the gully bottom is consistently the place where the largest errors occur; and these errors tend to be almost exclusively positive. Apart from the Celles gully, the maximum error measured in the DEMs are located on the gully bottom; these include some huge outliers. With the exception of the Brenas gully, the medians of the gully bottoms are much higher than the other geomorphologic classes. The median of the Brenas gully bottom does not appear to show the highest error. Although the slopes were steep, the gully bottom was quite wide so many of the test points were not taken as close to the slope of the gully as is the case in the other gullies. In addition, due to the tall grass on the flanks and the poor quality of one of the chunks, the other errors are higher. The flanks, which mostly consist of flat surfaces show incredible accuracies. Especially the Vailhes and Celles gullies, which have very little vegetation show good results. The errors on the slopes of the Celles and Vailhes gullies seem to be mostly negative, as opposed to the positive gully bottom errors. And, despite the relief the errors on the slopes are still considerably low. In the Brenas gully the slopes were one of the few places which were completely barren of vegetation, this explains the good accuracy scores there compared to the rest of the gully.

In all it can be said that the gully bottom point measurements appear to show the largest errors; errors which are almost exclusively positive. Meaning that the interpolated surface is higher at that location than in reality. Apparently the interpolation method has a hard time estimating the minimum points with respect to the higher points on the side. A curious phenomenon seems to occur on the slopes, errors in this class appear to be mostly negative. But they are still quite small compared to the errors at the gully bottoms. Figure 37 shows a generalization of the way a DEM created from UAV photometry compares to the actual surface according to the results.

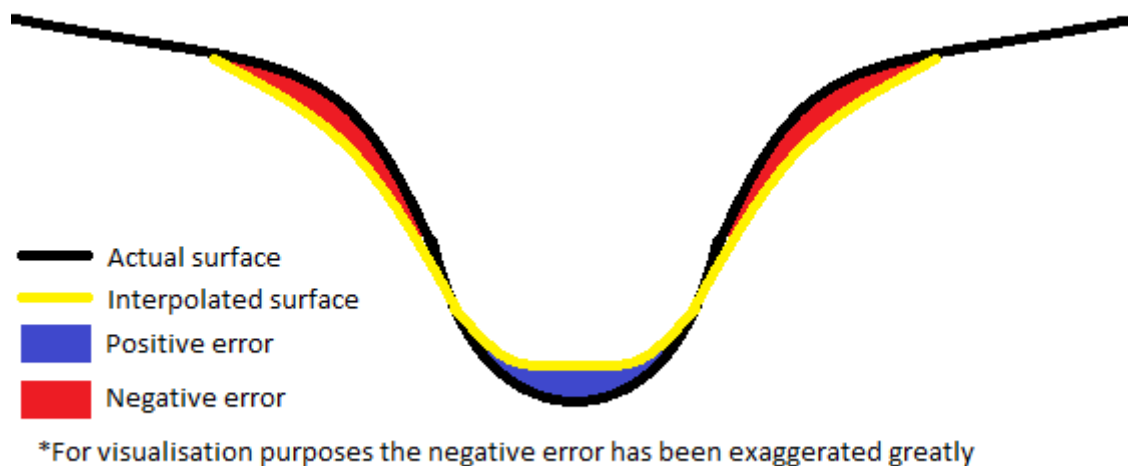


Figure 37 The DEM error relative to reality of a gully system

### *Comparing accuracy to other studies*

In this section the accuracies of the elevation models which can be found in appendix C will be compared to the accuracies of other elevation models created by other studies; these studies are described in detail in chapter 2.3.

In a study done by Hugenholtz et al. (2013) a DEM of 600 by 600 meters was made of parabolic dunes with 140 images and 26 GCPs. The study did not focus on relief so the height and relief of the dunes are not described in detail. The study describes a median of 0.07 meters and a RMS of 0.29 over 100 test points. Nearly all the test points are located in the area around the dunes, whereas in this study they have been put all throughout the gullies. Another major difference is how organized flight paths were used as opposed to the less organized ones used by this study, which was caused by the wind conditions. The accuracy results are roughly comparable to the accuracies reached in this study. For the high relief gullies (Brenas and Salagou) the medians are somewhat poorer (0.096 and 0.123) and the RMS (0.297 and 0.371) are roughly the same. The accuracies of the Vailhes and Celles gullies are however superior; however, the extend of those gullies is considerably smaller. The differences can also be the result of the different software which was utilized. They used Inpho by Trimble, while this study used Agisoft Photoscan.

Neitzel & Klonaski (2011) used Agisoft Photoscan to create a DEM of a flat parking lot and found an average elevation error of -0.025 meters which they attributed to the curvature effect which stems from the algorithm. The flanks of the Vailhes and Celles gullies are also relatively flat with little vegetation, comparable to the parking lot; their average errors are 0.011 and 0.025 respectively. Possible explanations for this difference between negative to positive errors are vegetation in the gully DEMs and most importantly, improvements in the Agisoft Photoscan software.

### 4.3 Discussing optimal settings

To obtain the optimal settings which were used for DEM creation in Agisoft Photoscan a series of tests was done. The different settings explored are Interpolation, depth filtering and amount of faces. The results are 18 different DEMs of the same area with different settings. Appendix H shows the statistics taken over all the test DGPS points and over all the different test runs. Appendix I shows the statistics for the reference points that were taken at the gully bottom level.

Depth filtering appears to be the most important factor contributing to model accuracy. An aggressive depth filter significantly increases the accuracy. Although there is no difference in the median, there is significant difference in the RMS and the size of the extremes. Large outliers point to severe errors in the DEM. Because the gullies can be considered as scenes with a complex geometry it is important to accurately represent the gully bottoms as they are thought to show the most errors. And because the end goal is to measure the gully volumes. Contrary to intuition the medians of the aggressive depth filtering mode, for the gully bottom, are actually slightly higher than those of the mild and moderate modes, however the RMS and the extremes are considerably lower.

Facecount does not seem to significantly affect the accuracy of the model. Of course the number should be enough to accurately represent the geometry of the scene. However, the amount of faces in the TIN can considerably increase processing times. And a large number of faces increases the demand on the computer to render graphics, when working with the models to implement the vegetation filter and the volume calculations. So a balance has to be found between the amount of faces and the ease of data management due to file size. This balance also depends on the extend of the scene, a large scene will require more faces for an accurate representation.

The interpolation method used(extrapolated or enabled) appears to be invariant for the accuracy of the resulting model. So the enabled setting is chosen because it is recommended by the program.

#### 4.4 Discussing volume analysis

The shape of the volume which is calculated resembles the shape of the gully. The shape is constrained on the bottom by the shape of the DEM, and at the top however the shape is governed by the manner in which the polygon indicating the gully extend is drawn. The latter is one of the determining factors in the error of the resulting volume measurement. Placing the edge to high or too low will significantly alter the final gully calculation, since the top of the gully also corresponds to its widest point, therefore those errors will have a large effect on the final gully volume calculation.

Determining where the edge of the gully is located sometimes requires best expert guessing, as a general rule the gully starts where there is a change in the gradient of the slope; this gradient change is often but not invariably coupled to a change in the type and amount of vegetation. This transition can also be smooth at some points making it hard to indicate the correct edge of the gully.

The Brenas gully has some eroding concave features at its head, which differ from the geomorphologic shape of the rest of the gully. Although these shapes are certainly caused at least in part by the same fluvial erosion which created the rest of the gully, they are not considered part of it. The slopes of these shapes transition seamlessly into the slopes of the area surrounding the gully. The transition between the gully and the second geomorphological stage is also hard to indicate on the east side of the Salagou gully .

Another point of uncertainty in the gully extend determination is the location of the end of the gully in the down slope direction. Ideally this would be an out flow point in a body of water or confluence with another larger gully system. The Salagou and Vailhes gullies both get wider at the end near the lake; the bottom is raised in these places because the gullies drain into the lake and are filled with sediment near the coastline. In the case of the Salagou gully the edges near the lake shore are less pronounced, especially on the east side where the edge corresponds to the top of a ridge. It should also be noted that the lake in question is an artificial lake so the true extend of the Vailhes an Salagou gullies remains unknown.

Despite its deficiencies the this method of gully volume calculation is still much more accurate than other older the methods.

## 5 Conclusions & recommendations

The volumes of four gullies located in the area around Salagou have been calculated using UAV photometry and GIS. In all 4 gullies of sizes, ranging from a relief of 100 meters and a width of 100 meters to and relief of 30 meters and width of 25 meters have been measured. The volumes range from  $10.95 \times 10^4$  cubic meters for the largest gully and  $1.17 \times 10^4$  cubic meters for the smallest gully. Gully formation in the area commenced as a result of climate changes at the end of the last glacial maximum. So the volumes reflect the amount eroded since the end of the Pleistocene era.

A method was presented to compute gully volumes using UAV photometry and GIS. From a hand launched UAV aerial photos were collected. And together with DGPS measurements Elevation models were made. Different settings in Agisoft Photoscan have been explored to gain the optimal settings for DEM creation. Using GIS the vegetation was removed, which should be done prior to computing the volumes, providing that it is not too dense. To achieve this a vegetation filter has been designed in the ArcGIS model builder. Gully volume calculations can be made by creating a 'lit' on top of the gully in GIS and subtracting the original gully morphology from this DEM, this yields the gully volume. When making the volume calculations, great care was taken in determining the edge of the gully, because the area at the top of is the largest errors here will also result in the largest errors in the volumes.

The accuracies of the elevation models of this study are on par with those of comparable studies. Accuracy analysis between the different geomorphologic features within gullies revealed that: an increase in the relief inside the gully drastically increases the errors in the gully bottom locations. These errors are by far most pronounced at the bottom of the gullies.

In general UAV photometry has proven to be a very promising new method in gully erosion research. Its accuracy and cost effectiveness allow for wide applicability. The created DEMs can be used for future research such as small scale catchment response analysis. In addition the making temporal measurements of the same gullies could yield erosion rates. And, these results could lend itself for an upscaling research concerning erosion rates of the wider area.



## Appendix A: Applications of UAVs

Ongoing technologic advances have led to miniaturization of both the platform and the payload. In addition the costs of unmanned aerial systems have been reduced significantly, this allowed for a rapid increase in private and commercial UAV use which is still. These developments have paved the way for a wide variety of new UAV applications. In this section a lot of but not all of the practical applications of UAVs will be listed. It expands on applications listed by Everaerts (2008), Watts et al. (2012) and Remondino et al. (2011)

The application of a UAV is dependent on the type of UAV and its payload. A UAV can carry various types of sensors: electro optical sensors of various bandwidth ranges like: near infrared, visible and hyperspectral. Conventional photographic images which also allow for 3D reconstruction using photometry. And, LiDAR or atmospheric sampling devices or radiation detection devices. A detailed list of applications of UAV photometry can be found in chapter 2.3.4.

- **Precision agriculture.** Larger rotary winged helicopters are used accurately spray the right pesticides without contaminating surrounding areas. In addition, infrared and hyperspectral sensors can be used to monitor crop health which allows for improved decision-making which can save money and time. And, accurate orthophotos have been used to determine the spacing between individual plants for optimum performance.
- **Forest monitoring.** hyperspectral meters and infrared can be used to monitor the state and health of trees. in addition, forest inventory can be mapped using high resolution imagery to map individual trees
- **Archeological mapping:** UAVs are a great tool to provide a bigger picture and increase our understanding of cultural heritage sites by creating 3D representations and 2D orthomosaics of them.
- **Wildlife survey.** Using thermal infrared and visible light sensors to track large-animals.
- **Mining surveys.** Creating 3D landscape models out of UAV imagery can be used to determine the volumes of stockpiles and open pit quarries. In addition hyper spectral images can be used to accurately explore new mining sites
- **Pipeline monitoring** hyperspectral sensors can be used to investigate the ground surrounding pipelines to determine leakage. In addition they can be used as a form of surveillance against illegal tapping in remote areas.
- **Precision dike monitoring.** Using UAVs to create high resolution 3D models of dikes and dams it can be assessed whether they meet safety requirements and regulations.
- **Plume tracking.** UAVs are well suited to tracking pollution plumes dependant on the type of pollutant different sensors should be used. It can track harmful substances without risk of injury to a pilot.
- **3D reconstruction of buildings.** City landscapes and individual objects can be accurately represented in 3D-models using LiDAR or stereoscopy. This can be done for a wide variety of applications like architecture and city planning.
- **Radiation measurement.** UAVs are undeterred by high levels of radiation so they are an excellent solution sparing human health in the case of a crisis
- **Disaster response.** Mapping the extent of disasters can be done very rapidly at low cost using UAVs.

## Appendix B: Python script for calculating statistics of a DEM

```
import csv
import os
from math import sqrt, fsum

# ----- define formulas -----

def average(lst):
    average = fsum(lst) / float(len(lst))
    return average

def variance(lst, average):
    rolling_sum = 0
    for i in lst:
        squared_dif = (average - i) ** 2
        rolling_sum += squared_dif
    variance = rolling_sum / len(lst)
    return variance

def std_deviation(variance):
    return sqrt(variance)

def median(lst):
    lst = sorted(lst)
    if len(lst) % 2.0 != 0:
        middle = len(lst) / 2.0 + 0.5
        return lst[int(middle) - 1]
    else:
        x = lst[len(lst) / 2]
        y = lst[len(lst) / 2 - 1]
        gem = (x + y) / 2.0
        return gem

def compute_rms(lst):
    total = 0
    for i in lst:
        squared = i ** 2
        total += squared
    rms = sqrt(total / float(len(lst)))
    return rms

def computeStatistics(lst, codeName, points, comparisonReport):
    ave = average(lst)
    var = variance(lst, ave)
    std = std_deviation(var)
    med = median(lst)
    rms = compute_rms(lst)
    print "statistics computed!"

    message = (
        "These are the statistics of the height errors for feature code %s which has %d sample points.\n" %
        (codeName, points)
        "\n" +
        "The average is: %f\n" % ave +
        "The median is: %f\n" % med +
        "The std_deviation is: %f\n" % std +
        "the rms is: %f\n" % rms +
        "the maximum error is: %f\n" % max(lst) +
        "the minimum error is: %f\n" % min(lst) +
        "\n"
    )
```

```

comparisonReport.write(message)
print "statistics written to file!"

# ===== The Program =====

# input files an parameters
path = raw_input("Where is the input located? (copy/paste path) :")
direc = os.path.dirname(path)
toRead = open (path, "r")
csvFile = csv.reader(toRead)

featureCode = 2   #input the column number for the feature code
modelHeight = [3] #input the column number for the model height, more than one columns are possible
DGPS = 1         #input the column number for the DGPS points

# run program
for col in modelHeight:
    toRead.seek(0)
    #initialize lists
    code1, code2, code3, code4, code5, allFeatures, allLists = [], [], [], [], [], [], []
    for index, row in enumerate(csvFile):
        if index == 0: #the first line contains the header
            name = row[col]
        elif not row[col]:
            print "no value"
        else:
            diff = float(row[col]) - float(row[DGPS])
            print diff
            if row[featureCode] != ("99" or "13"):
                allFeatures.append(diff)
                if row[featureCode] == "1":
                    code1.append(diff)
                elif row[featureCode] == "2":
                    code2.append(diff)
                elif row[featureCode] == "3":
                    code3.append(diff)
                elif row[featureCode] == "4":
                    code4.append(diff)
                elif row[featureCode] == "5":
                    code5.append(diff)
            elif row[featureCode] != ("99" or "13"):
                print "WARNING, this csv file inlcudes invalid feature codes!"

    allLists = [allFeatures, code1, code2, code3, code4, code5]
    newFile = direc + "\\ " + name + ".txt"
    report = open(newFile, 'w')
    report.write("This is the statistics report of project: %s" % name)
    report.write("\n")

    for index, i in enumerate(allLists):
        if not i:
            pass
        elif index == 0:
            points = len(i)
            codeName = "all"
            computeStatistics(i, codeName, points, report)
        else:
            points = len(i)
            codeName = str(index)
            computeStatistics(i, codeName, points, report)

    report.close()
toRead.close()

```

## Appendix C: Gully Tables

### Overview of gully geomorphology

Gully	Length	Max. Depth	Width	relief	Vegetation cover	slopes	Appendix
Brenas	450	25	100	100	Medium	Steep	G
Celles	320	8.5	30	50	Low	Mild	F
Salagou	250	30	70	70	High	Very steep	E
Vailhes	170	8.5	25	30	Low	Mild	D

### Overview of data used in the DEM creation

	Chunks	Aligned photos	GCPs
<b>Brenas</b>	<b>Combined</b>	<b>236</b>	<b>41</b>
	Lower	127	36
	Middle	40	11
	Upper	69	7
<b>Celles</b>	<b>Combined</b>	<b>79</b>	<b>40</b>
	Lower	36	21
	Upper	43	32
<b>Salagou</b>	<b>Combined</b>	<b>153</b>	<b>20</b>
	Lower	56	13
	Middle	58	16
	Upper	39	11
<b>Vailhes</b>	<b>Combined</b>	<b>94</b>	<b>23</b>
	Lower	51	10
	upper	43	19

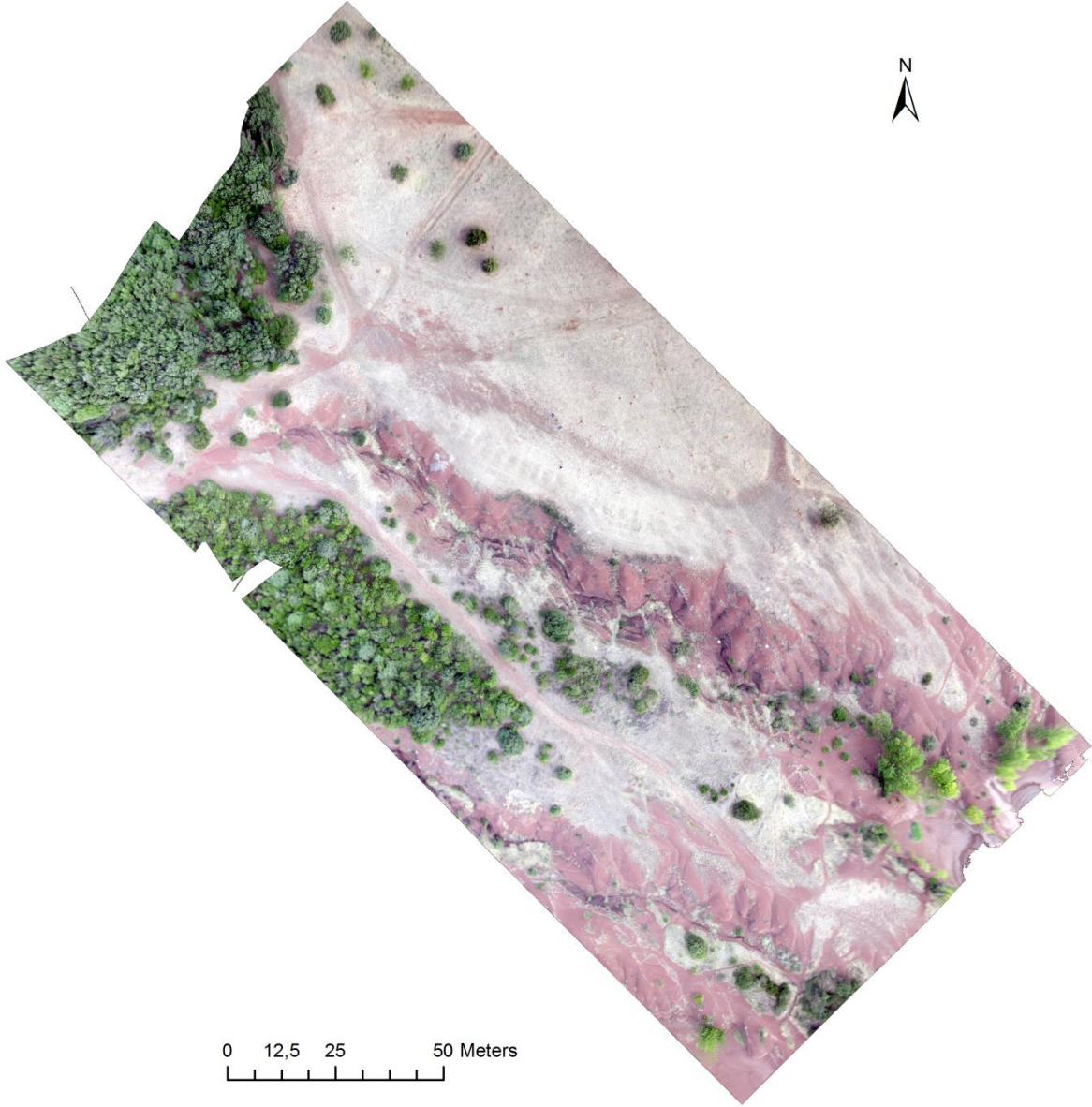
### Gully volumes and areas

Gully	Area	Volume(m <sup>3</sup> )	Olympic swimming pools	Average depth
<b>Brenas</b>	20105.05	109486.81	43.8	5.45
<b>Celles</b>	14386.16	40190.13	16.1	2.79
<b>Salagou</b>	14370.48	79730.89	31.9	5.55
<b>Vailhes</b>	5074.66	11735.81	4.6	2.31

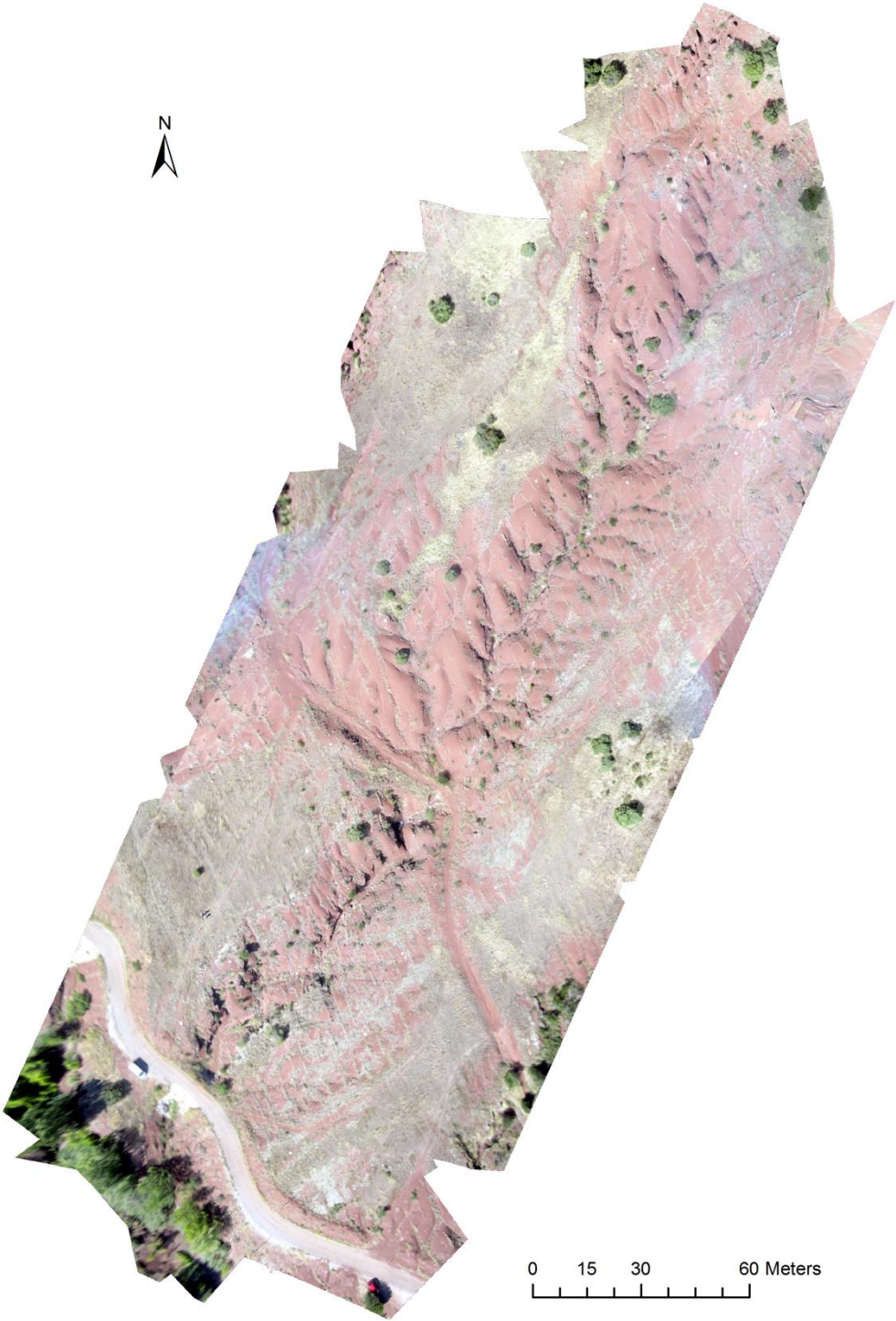
Gully DEM accuracies with respect to geomorphologic features

	geomorphology	control points	Average	median	STD	RMS	min	Max
<b>Brenas</b>		<b>159</b>	<b>0.178</b>	<b>0.123</b>	<b>0.237</b>	<b>0.297</b>	<b>-0.208</b>	<b>1.230</b>
	gully bottom	19	0.101	0.132	0.147	0.178	-0.169	0.439
	eastern flank	32	0.223	0.175	0.213	0.308	0.002	0.936
	western flank	56	0.143	0.122	0.185	0.234	-0.208	0.722
	slopes	25	0.172	0.107	0.29	0.337	-0.109	1.23
	central high	27	0.256	0.153	0.315	0.406	-0.05	1.213
<b>Celles</b>		<b>96</b>	<b>0.036</b>	<b>0.033</b>	<b>0.16</b>	<b>0.164</b>	<b>-0.5</b>	<b>0.528</b>
	gully bottom	24	0.088	0.059	0.122	0.15	-0.098	0.494
	flanks	42	0.025	0.023	0.155	0.157	-0.5	0.356
	slopes	30	0.009	-0.049	0.182	0.182	-0.275	0.528
<b>Salagou</b>		<b>59</b>	<b>0.162</b>	<b>0.096</b>	<b>0.333</b>	<b>0.371</b>	<b>-0.454</b>	<b>1.361</b>
	gully bottom	14	0.448	0.268	0.399	0.599	-0.01	1.361
	flanks	45	0.073	0.037	0.251	0.262	-0.453	0.731
<b>Vailhes</b>		<b>60</b>	<b>0.078</b>	<b>0.026</b>	<b>0.196</b>	<b>0.211</b>	<b>-0.22</b>	<b>0.82</b>
	gully bottom	20	0.23	0.159	0.252	0.341	-0.085	0.819
	flanks	25	0.011	0.007	0.085	0.086	-0.219	0.144
	slopes	15	-0.011	-0.038	0.107	0.107	-0.148	0.221

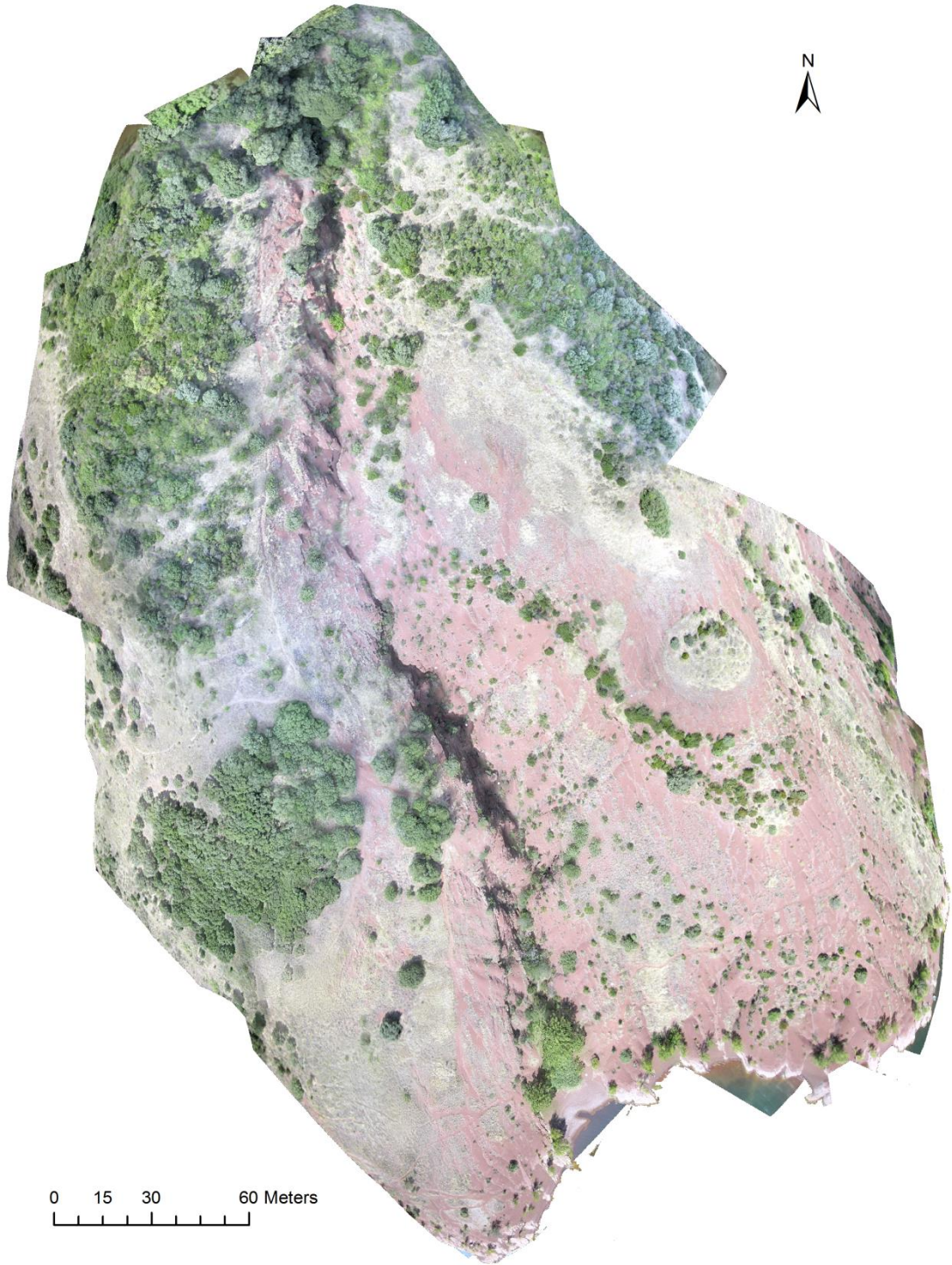
Appendix D: Orthophoto of the Vailhes gully



**Appendix E: Orthophoto of the Celles gully**

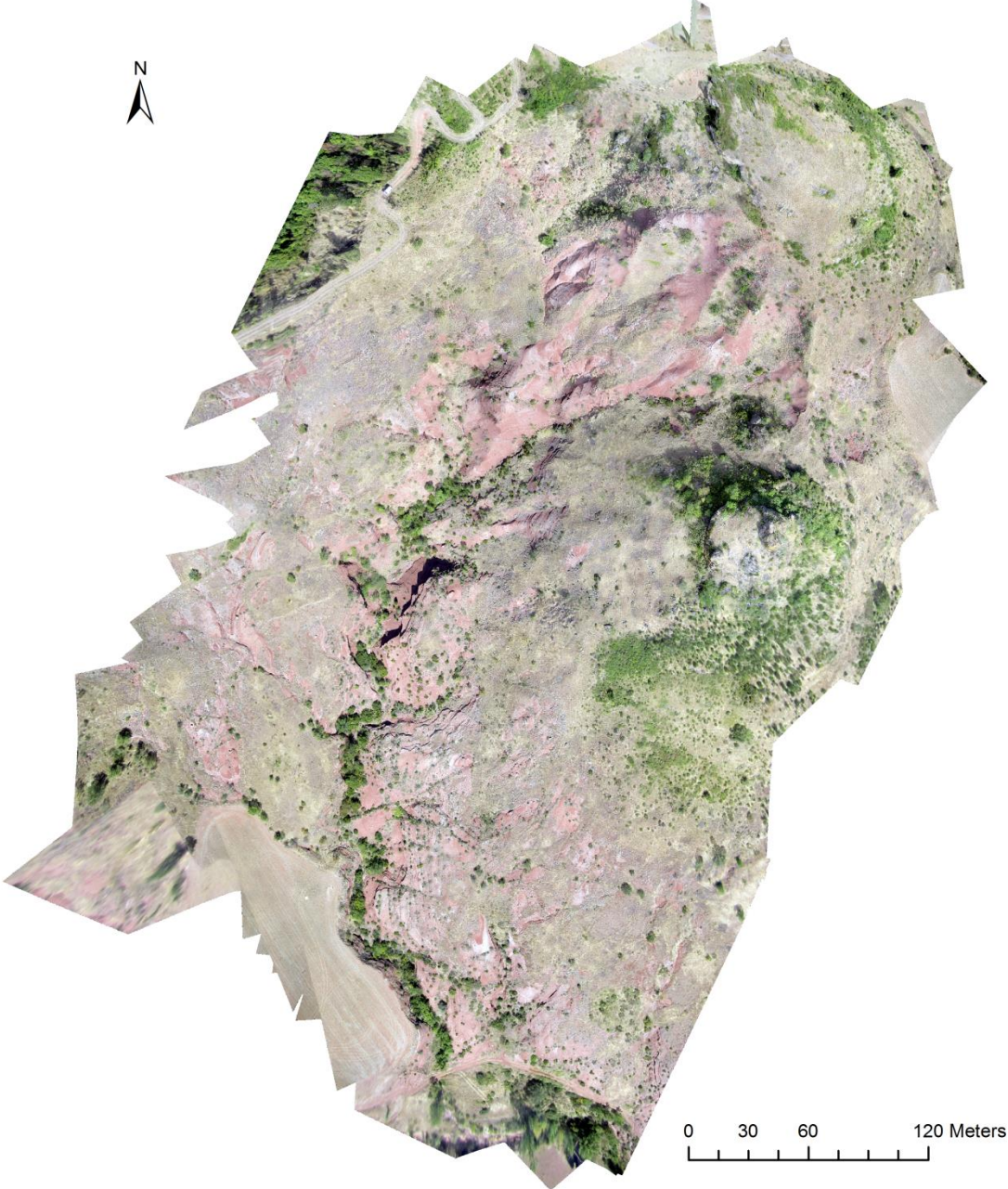


**Appendix F: Orthophoto of the Salagou gully**





Appendix G: Orthophoto of the Brenas gully



## Appendix H: Test run statistics (entire DEM)

Some parameters that were the same for all the runs were: The quality of the point cloud (medium) and the model type (height field). The statistics were computed from the difference between the models and DGPS at **60** reference points. The medium face count setting was roughly 150,000 faces and the high face count setting was roughly 550,000 faces.

Run number	Depth filtering	Interpolation	Face count	Average	Median	RMS	Maximum	Minimum
Run 7	Aggressive	Enabled	Medium	0,099936	0,042755	0,220051	0,87958	-0,21354
Run 8	Aggressive	Enabled	High	0,095118	0,043595	0,215155	0,85247	-0,21588
Run 9	Aggressive	Enabled	4 Million	0,094548	0,046225	0,215117	0,86054	-0,2221
Run 16	Aggressive	Extrapolated	Medium	0,094673	0,040905	0,217402	0,87477	-0,20927
Run 17	Aggressive	Extrapolated	High	0,094833	0,04364	0,21427	0,85158	-0,21893
Run 18	Aggressive	Extrapolated	4 Million	0,095132	0,046755	0,215248	0,86341	-0,22349
Run 1	Mild	Enabled	Medium	0,130338	0,042045	0,474622	3,41376	-0,24089
Run 2	Mild	Enabled	High	0,129987	0,036245	0,487624	3,53267	-0,23921
Run 3	Mild	Enabled	4 Million	0,129177	0,03817	0,486783	3,52419	-0,24328
Run 10	Mild	Extrapolated	Medium	0,130146	0,051055	0,457412	3,27854	-0,2254
Run 11	Mild	Extrapolated	High	0,131945	0,037075	0,484646	3,50769	-0,24528
Run 12	Mild	Extrapolated	4 Million	0,13201	0,03901	0,485356	3,51381	-0,24928
Run 4	Moderate	Enabled	Medium	0,104868	0,0433	0,294249	1,76619	-0,25557
Run 5	Moderate	Enabled	High	0,106142	0,04372	0,293218	1,76573	-0,27037
Run 6	Moderate	Enabled	4 Million	0,107286	0,04375	0,294921	1,7829	-0,26542
Run 13	Moderate	Extrapolated	Medium	0,108679	0,04484	0,292906	1,75099	-0,26201
Run 14	Moderate	Extrapolated	High	0,106229	0,04667	0,291024	1,75125	-0,25328
Run 15	Moderate	Extrapolated	4 Million	0,106592	0,04388	0,284454	1,68508	-0,25761

## Appendix I: Test run statistics (gully bottom)

The statistics were computed from the difference between the models and DGPS at **20** reference points, all the points which were located in the bottom of the gully. Some parameters that were the same for all the runs were: The quality of the point cloud (medium) and the model type (height field). The medium face count setting was roughly 150,000 faces and the high face count setting was roughly 550,000 faces.

Run number	Depth filtering	interpolation	Face count	Average	Median	RMS	Minimum	Maximum
Run 7	Aggressive	Enabled	Medium	-0,255084	-0,23335	0,354507	-0,87958	0,21354
Run 8	Aggressive	Enabled	High	-0,245246	-0,232595	0,346312	-0,85247	0,21588
Run 9	Aggressive	Enabled	4 Million	-0,244839	-0,234165	0,347187	-0,86054	0,2221
Run 16	Aggressive	Extrapolated	Medium	-0,251995	-0,23559	0,349079	-0,87477	0,20927
Run 17	Aggressive	Extrapolated	High	-0,244813	-0,232825	0,345412	-0,85158	0,21893
Run 18	Aggressive	Extrapolated	4 Million	-0,244454	-0,235435	0,347247	-0,86341	0,22349
Run 1	Mild	Enabled	Medium	-0,355625	-0,205855	0,810293	-3,41376	0,24089
Run 2	Mild	Enabled	High	-0,354411	-0,20211	0,83379	-3,53267	0,23921
Run 3	Mild	Enabled	4 Million	-0,35291	-0,18976	0,831987	-3,52419	0,24328
Run 10	Mild	Extrapolated	Medium	-0,351036	-0,21529	0,781398	-3,27854	0,2254
Run 11	Mild	Extrapolated	High	-0,355578	-0,197555	0,828813	-3,50769	0,24528
Run 12	Mild	Extrapolated	4 Million	-0,35546	-0,19896	0,830001	-3,51381	0,24928
Run 4	Moderate	Enabled	Medium	-0,286621	-0,219135	0,489679	-1,76619	0,25557
Run 5	Moderate	Enabled	High	-0,284989	-0,222495	0,489639	-1,76573	0,27037
Run 6	Moderate	Enabled	4 Million	-0,2855	-0,221085	0,492774	-1,7829	0,26542
Run 13	Moderate	Extrapolated	Medium	-0,292448	-0,24735	0,48914	-1,75099	0,26201
Run 14	Moderate	Extrapolated	High	-0,282443	-0,215485	0,485532	-1,75125	0,25328
Run 15	Moderate	Extrapolated	4 Million	-0,281466	-0,223215	0,47503	-1,68508	0,25761

## Appendix J

### **Preparing CSV files**

Sadly the trimble access software did not allow for proper exportation of data with the desired data in the correct columns as was needed for import in agisoft. For import of the GCP coordinates into Photoscan, the DGPS data needs to be supplied in a .txt or .csv format, in the form of a character separated value file; a file that contains rows data separated by a delimiting character like a comma or semi-colon do indicate the different columns. The reports of the GPS data exported from Trimble access contained the right information but in .html format. An open source program called CSVed and the windows text editor were used to extract the right information from the reports and convert them into the desired format.

## References

- Aber J.S., Marzolff I., Ries J.B., 2010. Chapter 13 - Gully Erosion Monitoring, *Small-Format Aerial Photography*, Elsevier, Amsterdam, 2010, Pages 193-200.
- Azhar M.N.A., Ahmad A., 2014. Development of Rapid & Low Cost Archaeological Site Mapping Using Photogrammetric Technique. *IOP Conf. Series: Earth and Environmental Science* 18.
- Barazzetti L., Remondino F., Scaioni M., 2010. Automation in 3D reconstruction: Results on different kinds of close-range blocks. *Int. Arch. Photogramm. Remote Sens. Spatial Inf. Sci.* 2010, 38, Part 5, p. 55–61.
- Bláha M., Eisenbeiss H., Grimm D., Limpach P., 2011. Direct georeferencing of UAVs. *International Archives of the Photogrammetry, Remote Sensing and Spatial Information Sciences*. Vol. XXVIII.
- Bertiger W., Desai S.D., Haines B., Harvey N., Moore A.W., Owen S., Weiss J.P., 2010. Single receiver phase ambiguity resolution with GPS data. *Journal of Geodesy*, Volume 84, Issue 5, pp 327-337
- Bocco G., 1991. Gully erosion, processes and models. *Progress in Physical Geography*, vol. 15, p.392–406.
- Bonnet S., Besnard M., Van den Driessche J., 2001. Drainage network expansion of the Salagou drainage basin (S. France): an example of relief response to recent climate change? *Terra Nova*, Volume 13, No. 3, p. 214-219.
- Buoncristiani J.F., Campy M., 2004. Paleogeography of the last two glacial episodes in the Massif Central, France. In J. Ehlers and P.L. Gibbard, *Quaternary glaciation – extend and chronology*. Published by Elsevier.
- Burrough, P. A., and R. A. McDonnell. 1998. *Principles of geographical information systems*. Oxford University Press, Oxford.
- Chaplot V., 2013. Impact of terrain attributes, parent material and soil types on gully erosion. *Geomorphology*, Volume 186, 15 March 2013, Pages 1-11.
- DeSIRE (2013, May 30) DeSIRE - Demonstration of Satellites enabling the Insertion of RPAS in Europe. <http://www.esa.int/ESA> Retrieved July 4, 2013 from: <http://iap.esa.int/projects/security/DeSIRE>
- Dotterweich M., Schmitt A., Schmidtchen A., Bork H.R., 2003. Quantifying historical gully erosion in northern Bavaria. *Catena* vol. 50, p. 135– 150.
- Eisenbeiss H. (2009). UAV Photometry. Unpublished doctoral dissertation. Eidgenössische Technische Hochschule (ETH), Zurich, Switzerland.
- Evans M.E., 2012. Magnetostratigraphy of the Lodève Basin, France: Implications for the Permo-Carboniferous reversed superchron and the geocentric axial dipole. *Studia Geophysica et Geodaetica*, 56 (3), pp. 725-734.

Evearts J., 2008. The use of unmanned aerial vehicles (UAVs) for remote sensing and mapping. *The International Archives of the Photogrammetry, Remote Sensing and Spatial Information Sciences*. Vol. XXXVII. Part B1. Beijing 2008 p. 1187-1192.

Frankl A., Nyssen J., De Dapper M., Haile M., Billi P., Munro R. N., Deckers J., Poesen J., 2011. Linking long-term gully and river channel dynamics to environmental change using repeat photography (Northern Ethiopia), *Geomorphology*, Volume 129, Issues 3–4, 15 June 2011, Pages 238-251.

Furukawa Y., Ponce J., 2010. Accurate, dense and robust multi-view stereopsis. *IEEE Transactions on Pattern Analysis and Machine Intelligence* 32(8), pp. 1362-1376.

Gastaud J., Campredon R. and Feraud G., 1983. Les systemes lioniens des Causses et du Bas Languedoc (sud de la France): geochronologie, relation avec les paleo-contraintes. *Bull. Soc. Geol. Fr.*, 7, p. 737-746.

Goesele M., Snavely N., Curless B., Hoppe H., Seitz S.M., 2007. Multi-view Stereo for Community Photo Collections. *Proceedings of ICCV 2007*, Rio de Janeiro, Brasil, October 14-20, 2007.

Hartley R., Zisserman A., (2004). *Multiple View Geometry in Computer Vision: Second Editino*. Cambridge University Press, Cambridge.

Harwin S., Lucieer A., 2012. Assessing the Accuracy of Georeferenced Point Clouds Produced via Multi-View Stereopsis from Unmanned Aerial Vehicle (UAV) Imagery. *Remote Sensing*, 4, p. 1573-1599.

Hoogtezicht (2013). Luchtvaartregels UAS en RPAS luchtvaartuig (drone). Retrieved from: <http://www.hoogtezicht.nl/wet-en-regelgeving/80-luchtvaartregels-voor-licht-onbemand-uas-en-rpas-luchtvaartuig-of-drone>, (accessed: 25 July 2013)

Hong Y., Fang J., Tao Y. (2008). Ground Control Station Development for Autonomous UAV. In *Intelligent Robotics and Applications* (pp. 36-44). Heidelberg: Springer Berlin.

Hugenholtz C.H., Whitehead K., Brown O.W., Barchyn T.E., Moorman B.J., LeClair A., Riddell K., Hamilton T., 2013. Geomorphological mapping with a small unmanned aircraft system (sUAS): Feature detection and accuracy assessment of a photogrammetrically-derived digital terrain model. *Geomorphology*, Volume 194, 15 July 2013, Pages 16-24.

Immerzeel W.W., Kraaijenbrink P.D.A., Shea J.M., Shrestha A.B., Pellicciotti F., Bierkens M.F.P., de Jong S.M., 2014. High-resolution monitoring of Himalayan glacier dynamics using unmanned aerial vehicles. *Remote Sensing of Environment* 150 (2014) 93–103

Leenheer M., 2006. *Soil Erosion in the Riverignes catchment: Application of the Revised Morgan-Morgan-Finney erosion model to a small Mediterranean catchment*. Master thesis, University of Utrecht, Netherlands.

Marzolf I., Poesen J., 2008. The potential of 3D gully monitoring with GIS using high-resolution aerial photography and a digital photogrammetry system, *Geomorphology*, Volume 111, Issues 1–2, 1 October 2009, Pages 48-60.

Morgan, R., & Davidson, D. (1986). *Soil erosion and conservation*. Essex, England: Longman Scientific & Technical

Neitzel F., Klonowski J., 2011. Mobile 3D mapping with a low-cost UAV system. *International Archives of the Photogrammetry, Remote Sensing and Spatial Information Sciences*, Volume 38 - 1, p. 39-44.

Newhall B., 1969. *Airborne camera: The world from the air and outer space*, Hasting House, Trowbridge & London, p. 144.

Niethammer U., James M.R., Rothmund S., Travelletti J., Joswig M., 2012. UAV-based remote sensing of the Super-Sauze landslide: Evaluation and results. *Engineering Geology*, Volume 128, 9 March 2012, Pages 2-11, ISSN 0013-7952, <http://dx.doi.org/10.1016/j.enggeo.2011.03.012>.

Nyssen J., Poesen J., Veyret-Picot M., Moeyersons J., Mitiku H., Deckers J., Dewit J., Naudts J., Kassa T., Govers G., 2006. Assessment of gully erosion rates through interviews and measurements: a case study from Northern Ethiopia. *Earth Surface Processes and Landforms*, vol. 31, p. 167–185.

Perroy R.L., Bookhagen B., Asner G.P., Chadwick O.A., 2010. Comparison of gully erosion estimates using airborne and ground-based LiDAR on Santa Cruz Island, California. *Geomorphology*, vol. 118, p. 288-300.

Piccarreta M., Capolongo D., Miccoli M.N., Bentivenga M., 2012. Global change and long-term gully sediment production dynamics in Basilicata, southern Italy. *Environmental Earth Science* 67, p. 1619–1630.

Poesen J., Vandekerckhove L., Nachtergaele J., Oostwoud Wijdenes D., Verstraeten G., van Wesemael B., 2002. Gully erosion in dryland environments. In: Bull L.J., Kirkby M.J. (eds) *Dryland rivers: hydrology and geomorphology of semi-arid channels*. Wiley, Chichester, pp 229–262

Poesen J., Nachtergaele J., Verstraeten G., Valentin C., 2003. Gully erosion and environmental change: importance and research needs. *CATENA*, Volume 50, Issues 2–4, 1 January 2003, Pages 91-133

Remondino F., Barazzetti L., Nex F., Scaioni M., Sarazzi D., 2011. Uav Photogrammetry for mapping and 3D modeling – current status and perspectives –. *Conference on Unmanned Aerial Vehicle in Geomatics*, Zurich, Switzerland.

Ramachandran M., Veeraraghavan A., Chellappa R., 2011. A Fast Bilinear Structure from Motion Algorithm Using a Video Sequence and Inertial Sensors. *Pattern Analysis and Machine Intelligence, IEEE Transactions on* , vol.33, no.1, pp.186,193, Jan. 2011.

Seitz S.M., Curless B., Diebel J., Scharstein D., Szeliski R., 2006. A Comparison and Evaluation of Multi-View Stereo Reconstruction Algorithms. *Computer Vision and Pattern Recognition, 2006 IEEE Computer Society Conference on* , vol.1, p.519-528.

Samani A.N., Wasson R.J., Malekian A., 2011. Application of multiple sediment fingerprinting techniques to determine the sediment source contribution of gully erosion: Review and case study from Boushehr province, southwestern Iran. *Progress in Physical Geography*, vol. 35 no. 3, p. 375-391.

Schneider J.G., Köner F., Roscher M., Kroner U., 2006. Permian climate development in the northern peri-Tethys area - the Lodève basin, French Massif Central, compared in a European and global context. *Paleogeogr. Paleoclimatol. Paleoecol.*, 240, p. 161-183.

Tice B.P., 1991. Unmanned aerial vehicles: the force multiplier of the 1990s. *Airpower journal*. Spring 1991.

Turner D, Lucieer A, Watson C. An Automated Technique for Generating Georectified Mosaics from Ultra-High Resolution Unmanned Aerial Vehicle (UAV) Imagery, Based on Structure from Motion (SfM) Point Clouds. *Remote Sensing*. 2012; 4(5):1392-1410.

Valcárcel M., Taboada M.T., Paz A., Dafonte J., 2003. Ephemeral gully erosion in Northwestern Spain. *Catena*, vol. 50, p. 199–216.

Valentin C., Poesen J., Li Y., 2005. Gully erosion: Impacts, factors and control. *CATENA*, Volume 63, Issues 2–3, 31 October 2005, Pages 132-153.

Watts, A. C., Ambrosia, V. G., & Hinkley, E. a. (2012). Unmanned Aircraft Systems in Remote Sensing and Scientific Research: Classification and Considerations of Use. *Remote Sensing*, 4(12), 1671–1692.

Xuelian Meng, Nate Currit and Kaiguang Zhao 3, 2010. Ground Filtering Algorithms for Airborne LiDAR Data: A Review of Critical Issues. *Remote Sensing* 2010, 2, 833-860 Zee van der W., Wibberley

C.A.J., Urai J.L., 2008. The influence of layering and pre-existing joints on the development of internal structure in normal fault zones: the Lodève basin, *France Geological Society, London, Special Publications*, 2008, 299:57-74.